HHS Public Access

Author manuscript

Nat Med. Author manuscript; available in PMC 2024 March 06.

Published in final edited form as:

Nat Med. 2022 September ; 28(9): 1860–1871. doi:10.1038/s41591-022-01960-7.

Post-infusion CAR T_{Reg} cells identify patients resistant to CD19-CAR therapy

Zinaida Good[1,2,3,†], **Jay Y. Spiegel**[1,4,†,^], **Bita Sahaf**[1], **Meena B. Malipatlolla**[1], **Zach J. Ehlinger**[1], **Sreevidya Kurra**[1,‡], **Moksha H. Desai**[1], **Warren D. Reynolds**[1], **Anita Wong Lin**[1,§], **Panayiotis Vandris**[1], **Fang Wu**[1], **Snehit Prabhu**[1], **Mark P. Hamilton**[1,4], **John S. Tamaresis**[2], **Paul J. Hanson**[1,4], **Shabnum Patel**[1,5], **Steven A. Feldman**[1,5], **Matthew J. Frank**[1,4], **John H. Baird**[1,4,Þ], **Lori Muffly**[1,4], **Gursharan K. Claire**[1,4], **Juliana Craig**[1,4,#], **Katherine A. Kong**[1], **Dhananjay Wagh**[6], **John Coller**[6], **Sean C. Bendall**[1,3,7], **Robert J. Tibshirani**[2,8], **Sylvia K. Plevritis**[1,2,9], **David B. Miklos**[1,4,*], **Crystal L. Mackall**[1,3,4,10,*]

[1]Center for Cancer Cell Therapy, Stanford Cancer Institute, Stanford University School of Medicine, Stanford, CA, USA.

[2]Department of Biomedical Data Science, Stanford University School of Medicine, Stanford, CA, USA.

[3]Parker Institute for Cancer Immunotherapy, Stanford University School of Medicine, Stanford, CA, USA.

[4]Division of Blood and Marrow Transplantation and Cellular Therapy, Department of Medicine, Stanford University School of Medicine, Stanford, CA, USA.

[5]Laboratory for Cell and Gene Medicine, Stanford University School of Medicine, Stanford, CA, USA.

[6]Stanford Genomics Facility, Stanford University School of Medicine, Stanford, CA, USA.

[7]Department of Pathology, Stanford University School of Medicine, Stanford, CA, USA.

[8]Department of Statistics, Stanford University, Stanford, CA, USA.

[9]Department of Radiology, Stanford University School of Medicine, Stanford, CA, USA.

[*]Corresponding author. cmackall@stanford.edu (C.L.M.); dmiklos@stanford.edu (D.B.M.).
[^]Present address: Sylvester Comprehensive Cancer Center, University of Miami, Miami, FL, USA.
[‡]Present address: Homer Stryker M.D. School of Medicine, Western Michigan University, Kalamazoo, MI, USA.
[§]Present address: Cancer Research Lab, Flow Cytometry Core Facility, University of California – Berkeley, Berkeley, CA, USA.
[Þ]Present address: Division of Lymphoma, Department of Hematology and Hematopoietic Cell Transplantation, City of Hope National Medical Center, Duarte, CA, USA.
[#]Present address: School of Medicine and Public Health, University of Wisconsin, Madison, WI, USA.
[†]These authors contributed equally.

Author contributions

C.L.M. and D.B.M. conceived the study, secured funding, and supervised the project; J.Y.S., M.J.F., J.H.B., L.M., G.K.C., J.C., K.A.K, M.P.H., P.J.H. and D.B.M. treated patients and/or acquired clinical samples and data; Z.G., M.B.M., P.V., B.S, A.W., and Z.E. designed and performed flow cytometry assays; S.P. and S.A.F. developed the qPCR assay; W.R. and B.S. performed the qPCR assay; M.B.M. and B.S. developed the panel and performed CyTOF with guidance from S.C.B. and Z.G.; Z.G., S.K., M.H.D., B.S., D.W., and J.C. developed and performed single-cell sequencing assays. Z.G., S.P., and M.P.H. analyzed CyTOF and single-cell sequencing data with advice from S.K.P. and J.C.; Z.G., J.Y.S., and J.S.T. analyzed the clinical, flow cytometry, and qPCR data and performed statistical analyses with advice from R.T.; Z.G., J.Y.S., D.B.M., and C.L.M. interpreted the results and wrote the first draft of the paper. All authors have critically reviewed the manuscript.

Competing interests

All other authors declare no competing interests.

[10]Department of Pediatrics, Stanford University School of Medicine, Stanford, CA, USA.

Abstract

Approximately 60% of patients with large B cell lymphoma (LBCL) treated with chimeric antigen receptor (CAR) T cell therapies targeting CD19 experience disease progression, and neurotoxicity remains a challenge. Biomarkers associated with resistance and toxicity are limited. Single-cell proteomic profiling of circulating CAR T cells in 32 patients treated with CD19-CAR identified that $CD4^+$ $Helios^+$ CAR T cells on day 7 post-infusion are associated with progressive disease and less severe neurotoxicity. Deep profiling demonstrated that this population is non-clonal and manifests hallmark features of T regulatory (T_{Reg}) cells. Validation cohort analysis upheld the link between higher CAR T_{Reg} cells with clinical progression and less severe neurotoxicity. A model combining expansion of this subset with lactate dehydrogenase (LDH) levels, as a surrogate for tumor burden, was superior for predicting durable clinical response compared to models relying on each feature alone. These data credential CAR T_{Reg} cell expansion as a novel biomarker of response and toxicity following CAR T cell therapy, and raise the prospect that this subset may regulate CAR T cell responses in humans.

Autologous CAR T cell therapies deliver sustained clinical benefit in less than half of patients treated with relapsed or refractory B cell malignancies, including large B cell lymphoma (LBCL)[1–3] and B cell acute lymphoblastic leukemia[4]. Axicabtagene ciloleucel (axi-cel), a commercially available CD19-CAR incorporating a CD28 costimulatory domain mediates disease control at 6 months in approximately 40% of LBCL patients, and disease progression following this timepoint is uncommon[5–8]. Neurological toxicity[9] occurs in two thirds of patients following axi-cel therapy and can be severe, causing seizures, cerebral edema, and in rare cases death[10]. Clinically validated biomarkers of disease progression and neurotoxicity are limited.

Current understanding of resistance to CD19-CAR therapies in LBCL implicates both inadequate CAR T cell potency and tumor resistance due to antigen modulation and potentially other mechanisms[11]. Polyfunctionality, increased stemness, and decreased exhaustion features of pre-infusion CAR T cells correlate with increased CD19-CAR T cell potency and increased rates of disease control[12–15]. On the tumor side, high pre-treatment tumor burden[1,5,15,16] associates with diminished disease control, likely due to induction of CAR T cell exhaustion, and potentially higher risk for antigen loss or other features associated with resistance to CAR T cell killing[17,18]. CAR T cell potency and tumor resistance are interdependent, since higher tumor burdens require greater CAR T cell proliferation and serial killing for tumor eradication, while diminished antigen expression may be overcome in some cases with higher potency CAR T cells[19,20]. Current concepts hold that CD19-CAR associated immune effector cell-associated neurotoxicity syndrome (ICANS) is linked to cytokine-mediated endothelial activation[21,22], ICANS-associated cells in infusion products[12], and possible on-target toxicity due to CD19 expression by brain mural cells[23], resulting in blood-brain barrier disruption and CAR T cell infiltration[10,22,24]. Biomarkers of severe neurotoxicity are limited[12,15,25,26].

Identification of biomarkers associated with increased risk of disease progression or severe neurotoxicity following CAR T cell therapy could enhance understanding of the biological basis for resistance and toxicity and enable earlier and potentially more effective treatment interventions. Several groups have measured circulating CAR T cell levels post-infusion using quantitative PCR (qPCR) or flow cytometry, and some studies have reported that higher peak or cumulative CAR T cell expansion associates with durable disease control or severe neurotoxicity[6,15], although a similar relationship was not found in other studies[2]. Here, using highdimensional single-cell proteomic profiling, we tested the hypothesis that post-infusion circulating CAR T cell subsets could identify patients at risk of disease progression or severe neurotoxicity following CD19-CAR therapy. In our discovery cohort, we studied peripheral blood CAR T cells from 32 LBCL patients receiving commercial axi-cel. Data-driven analyses identified three populations of CAR T cells circulating on day 7 post-infusion that associated with durable disease control or severe neurotoxicity. A higher frequency of $CD4^+$ CAR T cells expressing Helios on day 7 post-infusion associated with lower rates of severe neurotoxicity and a higher likelihood of disease progression. These cells were non-clonal and exhibited a T regulatory (T_{Reg}) cell phenotype, with expression of FOXP3 and CD25. Prospective study of a second validation cohort comprising 31 LBCL patients confirmed that increased CAR T_{Reg} cells early after infusion predict clinical progression and a lowered risk for severe neurotoxicity. Frequency of CAR T_{Reg} cells was inversely correlated with total CAR T cell expansion, but did not correlate with tumor burden quantified by lactate dehydrogenase (LDH) levels. A model combining CAR T_{Reg} and LDH levels was superior for predicting clinical response than each feature alone. Together, these data implicate post-infusion CAR T cells with hallmarks of regulatory T cells in modulating response and toxicity following CAR T cell therapy.

Results

Circulating CAR T cell counts do not associate with response

We studied 32 consecutive LBCL patients treated with commercial axi-cel at Stanford Hospital between December 1, 2017 and November 1, 2018 and followed until March 3, 2020 (Fig. 1a and Supplementary Table S1). Despite comorbidities that would have rendered 12 of these patients ineligible for the ZUMA-1 trial[3] and other differences (Supplementary Table S2), progression-free survival (PFS) and overall survival (OS) were similar between the Stanford and ZUMA-1 cohorts, and similar to ZUMA-1, relapses following 6 months were rare[6] (Fig. 1b).

A flow cytometry assay incorporating an antibody that specifically detects the FMC63 scFv target-binding domain in axi-cel[27] was used to measure circulating CAR T cells sequentially post-infusion (Fig. 1a,c). Median CAR T cell expansion peaked at 28.2 CAR T cells/μL on day 7 and steadily declined thereafter (Fig. 1d), with similar behavior of $CD4^+$ and $CD8^+$ CAR^+ T cell subsets (Extended Data Fig. 1a) and significant correlation between flow cytometry and qPCR tracking of circulating CAR T cell numbers (Fig. 1e). CAR T area under the curve (AUC) or area under the moment curve (AUMC) quantified for days 0–28 did not differ significantly between patients with complete response (CR) or progressive disease (PD) at 6 months (Fig. 1f and Extended Data Fig. 1b) and did not significantly

associate with the best response (Extended Data Fig. 1c). Similarly, neither CAR T cell peak expansion nor expansion on day 7, 14, 21 or 28 was associated with clinical response at 6 months (Extended Data Fig. 1d,e). These results were confirmed with qPCR (Extended Data Fig. 1f-h).

Maximum cytokine release syndrome (CRS) was grade 2 (Fig. 1a), and we therefore could not study high-grade CRS, although higher CAR T cell levels were associated with higher CRS (Extended Data Fig. 1i,j), as previously reported[28]. ICANS occurred later than CRS (max CRS: day 0–8, max ICANS: day 4–12), and severe ICANS (grade 2–4) was significantly associated with CAR T $AUC_{0–28}$, $AUMC_{0–28}$, peak levels, and CAR expansion on day 21 and day 28 (Fig. 1g and Extended Data Fig. 1k,l). In summary, higher post-infusion CAR T cell levels did not associate with disease control but did associate with CRS and severe neurotoxicity.

Three metaclusters associate with response or neurotoxicity

Mass cytometry by time-of-flight (CyTOF) enables high-throughput proteomic monitoring of single-cell phenotypes[29]. To identify whether expansion of specific CAR T cell subsets associates with clinical response, we used CyTOF to assess expression of 34 surface or intracellular markers relevant to T cell function (Fig. 2a and Supplementary Table S3) and 14 quality control parameters (Methods). Batched blood samples collected prior to axi-cel infusion, on day 7 (peak expansion), and on day 21 post-infusion (late expansion) from 31 patients were analyzed. In this study, we did not have access to the commercial axi-cel infusion products for analysis.

We focused our analysis on day 7 post-infusion, the time of peak CAR T cell expansion (Fig. 1d). Single-cell clustering identified 25 clusters of day 7 circulating CAR T cells that were grouped automatically into 10 metaclusters (Fig. 2b,c). Clusters were connected to their most similar neighbors based on average marker expression, forming a minimum spanning tree. To pinpoint potentially predictive metaclusters for CR *vs.* PD at 6 months, we built a lasso model and applied 10-fold cross-validation to estimate its performance on unseen samples (Fig. 2d). Lasso is a multivariate regression model that utilizes sparsity to select a set of features that together can predict a given response[30]. Cross-validation identified optimal model performance at $\lambda = 0.102$, corresponding to 3 metaclusters (Fig. 2e). Relative abundance of CAR T cells in each metacluster and b coefficients of the final lasso model identified metaclusters 3 and 6 as predictive of CR at 6 months, whereas metacluster 4 was predictive of PD at 6 months (Fig. 2f). The magnitude of β coefficients indicates relative importance of each metacluster, while the sign specifies its class (negative for CR, positive for PD).

Relative to other CAR T cells, the two metaclusters associated with CR were $CD57^+$ subsets of $CD4^+$ (metacluster 3) and $CD8^+$ (metacluster 6) CAR T cells that were enriched for Blimp-1 and T-bet transcription factors, but not the exhaustion marker CD39 (Fig. 2g and Extended Data Fig. 2). Inhibitory proteins PD1, LAG3, and TIM3, which are linked to activation and exhaustion, were expressed at lower levels in the $CD8^+$ $CD57^+$ subset (metacluster 6), and CD28 was also expressed at lower levels in this subset, as previously reported[31]. Metacluster 3 also expressed high levels of PD1 and ICOS, suggesting similarity

to T follicular helper (T_{FH}) cells. In contrast, metacluster 4, which associated with PD, comprised Helios$^+$ CD4$^+$ CAR T cells that expressed high levels of CD25, CTLA4, and TIGIT, indicating similarity to an immunosuppressive T_{Reg} subset. All three metaclusters expressed Ki-67, a marker of proliferating cells, in at least one of their clusters, indicating that at least a fraction of the cells had recently cycled or were continuing to cycle. Differential abundance analysis[32] confirmed these results and also identified CAR T cells with exhaustion features, including CD39, CD101, and CD244 expression, as associated with PD at 6 months (Extended Data Fig. 3).

We repeated the lasso analysis to identify day 7 metaclusters of circulating CAR T cells associated with severe neurotoxicity (Fig. 2h). Here, optimal model performance was achieved at $\lambda = 0.090$, corresponding to 2 metaclusters (Fig. 2i). The final model's β coefficients and relative abundance of CAR T cells revealed that metaclusters 4 and 8 were associated with reduced neurotoxicity (Fig. 2j). Metacluster 4 was of special interest, because it was the same metacluster associated with PD at 6 months and contained CD4$^+$ CAR T cells with T_{Reg}-associated protein expression. Metacluster 8 was similar to metacluster 6, as it contained CD57$^+$ CD8$^+$ CAR T cells enriched for Blimp-1 and T-bet, but it also displayed features of exhaustion, including CD39, CD101, and CD244 expression. These findings were consistent with the results of differential abundance analysis (Extended Data Fig. 4).

Together, single-cell proteomic analyses of day 7 circulating CAR T cells in patients treated with axi-cel for LBCL identified three metaclusters that distinguished patients with long-term clinical response and two metaclusters associated with severe neurotoxicity. CD4$^+$ T cells bearing hallmarks of regulatory T cells correlated in both analyses, being increased in patients with less severe neurotoxicity and those experiencing progressive disease, while CD4$^+$ and CD8$^+$ CAR T cells bearing a T effector (T_{EFF}) phenotype with senescence features were increased in patients who experienced durable disease control.

CAR T_{Reg} cells linked to progression and lower neurotoxicity

Because cell assignment into metaclusters relies on all 31 markers used for clustering (Fig. 2c), we tested whether a simplified gating strategy utilizing the salient proteins identified in the metaclusters would associate with clinical response at 6 months in the CyTOF dataset (Fig. 3a). We confirmed that on day 7 post-infusion, CD4$^+$ and CD8$^+$ subsets of CD57$^+$ T-bet$^+$ CAR T cells were significantly higher in patients experiencing CR at 6 months, whereas CD57$^-$ Helios$^+$ CD4$^+$ CAR T cells were higher in patients with PD (Fig. 3b). Notably, no difference in levels of these subsets was present prior to axi-cel infusion in patients who experienced CR *vs.* PD (Extended Data Fig. 5a). At day 21 post-infusion, CAR T cells showed trends similar to those observed at day 7 (Extended Data Fig. 5b). We also saw significantly higher levels of CAR-negative CD57$^+$ T-bet$^+$ T cells in patients with durable CR, which could include CAR-transduced cells which have downregulated their receptor[33] and/or may indicate stronger lymphopenia-induced expansion in responding patients (Extended Data Fig. 5c,d). We next assessed relationships between each CAR T cell population (separated by dotted lines, Fig. 3b) and time to progression (TTP) using Kaplan-Meier analysis, and observed significant differences in TTP between patients divided into

two groups based upon high *vs.* low expansion of each population (Fig. 3c). Although TTP and PFS results are identical here, we used TTP for subsequent analyses to avoid confounding results due to death from infection or causes unrelated to LBCL.

To assess whether a simplified gating strategy would identify correlations between higher T_{Reg}-like CAR T cells and less severe neurotoxicity, we examined $CD4^+$ CAR T cells in the $CD57^-$ $Helios^+$ gate (Fig. 3a,d) and confirmed significantly lower frequencies of $CD4^+$ $CD57^-$ $Helios^+$ CAR T cells in patients with severe neurotoxicity (Fig. 3e). Of note, a gate based on metacluster 8 was not significantly associated with severe neurotoxicity (Extended Data Fig. 5e,f), which is consistent with its lower coefficient magnitude ($\beta = -2.17$), as compared to metacluster 4 ($\beta = -5.31$) in the lasso model (Fig. 2j). We did not observe differences in the frequency of the circulating $CD57^-$ $Helios^+$ population among $CD4^+$ T cells prior to axi-cel infusion in patients stratified by severe neurotoxicity, nor among $CD4^+$ CAR T cells on day 21, at which time neurotoxicity was largely resolved (Extended Data Fig. 5g). Notably, both $CD57^+$ $T\text{-}bet^+$ populations of $CD4^+$ and $CD8^+$ CAR T cells on day 7, which were associated with durable CR, had no association with neurotoxicity (Fig. 3f).

Cytomegalovirus (CMV) is a common pathogen, and chronic CMV infection has been implicated in the accumulation of $CD57^+$ T cells[34]. We observed a significantly higher frequency of circulating $CD57^+$ T cells in patients with evidence for prior CMV infection prior to axi-cel infusion (Extended Data Fig. 6a), although these differences became less pronounced in CAR-negative T cells post-infusion, likely due to lymphopenia-induced proliferation (Extended Data Fig. 6b,c). CMV status was not significantly associated with any of the $CD57^+$ populations examined among CAR T cells on days 7 and 21 (Extended Data Fig. 6d,e) and did not associate with TTP or OS in this cohort (Extended Data Fig. 6f).

Together, these results establish relationships between three easily defined populations of circulating CAR T cells on day 7 and long-term clinical outcome or severe neurotoxicity in LBCL patients treated with commercial axi-cel. Early expansion of circulating T_{Reg}-like CAR T cells associates with both disease progression and lower levels of severe neurotoxicity, whereas $CD57^+$ $T\text{-}bet^+$ populations associate with greater disease control.

CAR T_{Reg} cells express FOXP3 and lack cytotoxic potential

We next sought to interrogate the functional properties of the three identified CAR T cell populations in response to activation. Peripheral blood mononuclear cells (PBMCs) were stimulated either using small molecule mimics of TCR signaling (PMA and ionomycin), or through CAR (using plate bound anti-FMC63 antibody) for 6 hours prior to analysis by intracellular flow cytometry, with gating on CAR^+ populations. As controls, we utilized healthy donor-derived T cells analyzed at baseline and following transduction with a retroviral construct encoding a CD19-CD28ζ CAR, thereby replicating the axi-cel construct. As expected, prior to transduction $CD4^+$ $CD57^+$ $T\text{-}bet^+$ T cells were nearly absent and $CD4^-$ $CD57^+$ $T\text{-}bet^+$ T cells were infrequent (Extended Data Fig. 7a). Among CD19-CD28ζ CAR-transduced T cells analyzed on day 11 or 12 in culture, $CD57^+$ $T\text{-}bet^+$ $CD4^+$ and $CD4^-$ CAR T cells were rare (Extended Data Fig. 7b), in agreement with prior reports that CAR T cells in the infusion product typically do not express CD57[35]. $CD57^-$ $Helios^+$ cells were detectable both in healthy donor $CD4^+$ T cells and in CD19-CD28ζ CAR-transduced $CD4^+$

T cells. Of note, we observed a large FOXP3^{+} CD25^{High} population among CD19-CD28ζ CAR-transduced CD4^{+} T cells, which did not express Helios, in contrast to CD4^{+} T cells from healthy donors (Extended Data Fig. 7c).

Intracellular flow cytometry of cryopreserved day 7 post-infusion PMBCs from 27 patients revealed that all three populations were readily detectable following activation (Fig. 4a, Extended Data Fig. 7d). The CD4^{+} CD57^{-} Helios^{+} population expressed both CD25 and FOXP3, a key transcription factor of T_{Reg} cells, and did not produce IL-2 following activation (Fig. 4a-c). The CD57^{+} T-bet^{+} populations were strong producers of granzyme B (GZMB), a cytotoxic granule protein, and CD8^{+} CD57^{+} T-bet^{+} cells expressed the largest amount of surface CD107a, a marker of recent degranulation. The CD4^{+} CD57^{+} T-bet^{+} populations did not produce IL-2, whereas a small fraction (median 3.1%) of CD4^{-} CD57^{+} T-bet^{+} population produced IL-2 in response to CAR activation only. These data demonstrate that the CD4^{+} CD57^{-} Helios^{+} CAR T cell population is phenotypically similar to T_{Reg} cells, providing a basis for its association with progressive disease and reduced neurotoxicity. In contrast, GZMB is expressed by the majority of CD4^{-} CD57^{+} T-bet^{+} (mean ± SEM: 65.8 ± 6.8%) and a large fraction of CD4^{+} CD57^{+} T-bet^{+} (35.5 ± 9.0%) CAR T cells, consistent with high cytotoxic potential, potentially explaining their association with durable CR.

CAR T_{Reg} cells are polyclonal with T_{Reg} gene signature

To more deeply characterize the outcome-associated CAR T cell populations, we performed single-cell RNA-sequencing (scRNA-seq) with targeted single-cell T cell receptor sequencing (scTCR-seq) of sorted CAR^{+} T cells from nine LBCL patients on day 7 following axi-cel infusion (Fig. 5a,b and Supplementary Table S1). As CD57 itself is not encoded by a gene, but rather represents a carbohydrate epitope induced by the beta-1,3-glucuronyltransferase 1 (B3GAT1) enzyme, we performed antibody-based single-cell surface analysis by cellular indexing of transcriptomes and epitopes by sequencing (CITE-seq)[36] to resolve single-cell expression of CD57, as well as a panel of 42 surface proteins (Supplementary Table S3). We found that CD4^{+} CD57^{-} Helios^{+} CAR T cells were enriched for *FOXP3*, *IL2RA*, *TIGIT*, *CTLA4*, and *RTKN2* at the transcript and/or surface protein level, consistent with our prior data and their T_{Reg} phenotype (Fig. 5c-g and Extended Data Fig. 8). Further, CD4^{+} CD57^{-} Helios^{+} CAR T cells were similar to CD4^{+} FOXP3^{+} CAR T cells, and to those classified as T_{Reg} by projecting our data onto an annotated reference dataset from blood of healthy donors using *Azimuth*[37] (Fig. 5e). Systematic differential gene expression and pathway analyses identified T_{Reg} development as one of the top enriched pathways when we compared CD4^{+} CD57^{-} Helios^{+} cells to both CD57^{+} T-bet^{+} populations, each CD57^{+} T-bet^{+} population separately, or all other CAR T cells (Fig. 5f and data not shown).

Both CD4^{+} and CD8^{+} subsets of CD57^{+} T-bet^{+} CAR T cells expressed high levels of *GZMA*, *GZMB*, *GZMH*, *PRF1*, and *NKG7*, consistent with a cytolytic T_{EFF} state (Fig. 5c-g and Extended Data Fig. 8). Although CD4^{+} CD57^{+} T-bet^{+} CAR T cells resembled T_{FH} cells based on our CyTOF data, they did not express *BCL6*, which encodes a key transcription factor in T_{FH} cell differentiation (2.8% BCL6^{+}; Extended Data Fig. 8d).

Based on their mRNA expression of *TBX21* (T-bet transcription factor) and *CD40LG* (CD40L co-stimulatory receptor), $CD4^+$ $CD57^+$ $T\text{-}bet^+$ CAR T cells displayed similarities to both T_H1 and T_{EFF} cells, whereas $CD8^+$ $CD57^+$ $T\text{-}bet^+$ CAR T cells most closely resembled T_{EFF}. T cell senescence is characterized by expression of CD57 and loss of CD28 by $CD8^+$ T effector memory (T_{EM}) cells, some of which re-express CD45RA (T_{EMRA})[34,38]. $CD8^+$ $CD57^+$ $T\text{-}bet^+$ CAR T cells identified here expressed reduced levels of CD27 and CD28 (Fig. 5g and Extended Data Fig. 8d-f) and contained a T_{EMRA} subset (22.0% *vs.* 8.5% for $CD4^+$ $CD57^+$ $T\text{-}bet^+$, 0.6% for $T\text{-}_{Reg}$-like, and 10.1% for other CAR T cells). However, the majority of $CD57^+$ $T\text{-}bet^+$ CAR T cells identified here did not demonstrated increased mRNA expression of other senesce-associated genes *CDKN1A* (P21), *CDKN2A* (P16), *GLB1* (β-galactosidase), and *USP16* (Extended Data Fig. 8d,f), indicating that these populations may not have reached terminal senescence. Both $CD4^+$ and $CD8^+$ populations of $CD57^+$ $T\text{-}bet^+$ CAR T cells expressed variable levels of *PDCD1* (PD1) and *HAVCR2* (TIM3) inhibitory receptors, and low mRNA levels of *TOX* (TOX)[39–42], *NR4A2* (NR4A2)[43], and *ENTPD1* (CD39)[44] terminal T cell exhaustion markers. Together, the profile of the $CD57^+$ $T\text{-}bet^+$ cells identified here closely resembles that described in terminally differentiated effector T cells with early senescence features, rather than exhausted T cells.

Cell cycle analysis using 97 canonical cell cycle markers[45] showed that all three populations contained a subset of proliferating cells (18–26%; Extended Data Fig. 8g). TCR clonotype analysis revealed that $CD4^+$ $CD57^-$ $Helios^+$ CAR T cells consistently demonstrated high repertoire diversity and were mostly composed of unique TCR clones. In contrast, both $CD57^+$ $T\text{-}bet^+$ CAR T cell populations comprised highly clonally expanded cells (Fig. 5h). Altogether, single-cell transcriptomic and proteomic profiling conducted alongside clonality analysis demonstrated that $CD4^+$ $CD57^-$ $Helios^+$ CAR T cells, which associated with poor disease control and diminished neurotoxicity, were largely clonally unique cells that demonstrated hallmark features of regulatory T cells. In contrast, $CD4^+$ and $CD8^+$ populations of $CD57^+$ $T\text{-}bet^+$ CAR T cells comprise clonally expanded cells with high cytotoxic potential.

CAR T_{Reg} validation and evidence of *in vivo* suppression

To validate our findings, we prospectively analyzed a cohort of 31 additional LBCL patients treated with axi-cel at our institution between November 2, 2018 and July 1, 2021 and followed until February 17, 2022 (Supplementary Table S1). The baseline demographics of our validation cohort were similar to our discovery cohort (Supplementary Table S4). Cryopreserved PMBCs collected on day 7 post-infusion from this second patient cohort were examined using flow cytometry (Supplementary Table S3). These data confirmed that CAR T_{Reg} cells were associated with PD at 6 months and lower neurotoxicity, with nearly identical results for $CD57^-$ $Helios^+$, $CD57^-$ $FOXP3^+$, and $CD57^-$ $Helios^+$ $FOXP3^+$ subsets of $CD4^+$ CAR T cells (Fig. 6a,b). When we separated patients into groups with high and low $CD4^+$ $CD57^-$ $Helios^+$ (T_{Reg}-like) CAR T cell fractions using the threshold from the discovery cohort (12%; dotted line in Fig. 3b), we observed significant differences in TTP using Kaplan-Meier analysis (Fig. 6c), with results matching those seen earlier (Fig. 3c).

We further sought to determine whether there was additional evidence of immune suppression by CAR T_{Reg} cells *in vivo*. An important T_{Reg} mechanism of action is suppression of T cell proliferation, especially within the effector $CD8^+$ subset. Here, analysis of all available data showed a clear inverse and significant correlation between the CAR T_{Reg} fraction and CAR T cell expansion (Extended Data Fig. 9a), with the strongest trend observed within $CD8^+$ CAR T cells (Fig. 6d). We also observed a trend of delayed peak neurotoxicity in patients with higher CAR T_{Reg} fraction on day 7 when stratified by ICANS severity (Extended Data Fig. 9b).

Higher levels of $CD57^+$ T-bet^+ cells measured by flow cytometry in the validation cohort did not associate with improved outcomes (Extended Data Fig. 9c). The basis for this lack of validation is not entirely clear, but close examination revealed that $CD57^+$ T-bet^+ populations were nearly mutually exclusive with CAR T_{Reg} population in the discovery cohort (Extended Data Fig. 9d and data not shown), whereas in the validation cohort, a significant fraction of $CD57^+$ T-bet^+ cells expressed Helios in patients who progressed (Extended Data Fig. 9e). We therefore compared $Helios^+$ to $Helios^-$ CAR T cells within the $CD57^+$ T-bet^+ population using our single-cell sequencing data. $Helios^+$ $CD57^+$ T-bet^+ cells did not express T_{Reg} markers *FOXP3*, *IL2RA*, or *RTKN2*, but were enriched for expression of *TIGIT* and markers of natural killer (NK) cells (Extended Data Fig. 9f-h), indicating similarity to the NK-like subset recently associated with poor outcomes following CAR T cell therapy[46]. Thus, we observed heterogeneity within $CD57^+$ T-bet^+ CAR T cells that appears relevant to clinical response, suggesting that these populations may include multiple cell states.

Synergy between CAR T_{Reg} cells and a tumor burden surrogate

In both discovery and validation cohorts, we observed a few patients who progressed despite having a low fraction of CAR T_{Reg} cells (Fig. 3b and Fig. 6a). Increased pre-lymphodepletion LDH level, which provides a surrogate for tumor burden, has emerged as a key correlate of progression[5]. We therefore examined CAR T_{Reg} cell levels in the context of LDH and other clinical parameters. CAR T_{Reg} fraction was not significantly correlated to LDH (Extended Data Fig. 10a) and was similar in patients with normal or high LDH (Extended Data Fig. 10b). However, both $CD4^+$ $CD57^-$ $Helios^+$ CAR T cell and LDH levels effectively distinguished patients with CR or PD at 6 months (Fig. 6e). Moreover, patients who progressed at 6 months had more circulating CAR T_{Reg} cells than those in CR at 6 months in both low and high LDH groups (Extended Data Fig. 10c). Therefore, high LDH and CAR T_{Reg} fraction are two independent determinants of clinical progression, prompting us to combine these two features in a logistic regression model (Fig. 6f). We fit this model and identified an optimal classification threshold using the discovery cohort, and then tested on the validation cohort, with excellent performance in both cohorts (Fig. 6g). We used the model risk (Supplementary Table S5) to stratify patients for Kaplan-Meier analysis and observed that low-risk patients have a significantly better TTP (Fig. 6h) and OS (Fig. 6i). Notably, this model had better predictive performance with superior TTP and OS separation than models using each feature alone (Extended Data Fig. 10d-g).

Together, these results demonstrate that increased CAR T_{Reg} cells circulating early post-infusion predict clinical progression and mild neurotoxicity, and provide evidence for diminished CAR T cell expansion in patients with high circulating CAR T_{Reg} cells. Combining a tumor burden surrogate with enumeration of post-infusion CAR T_{Reg} cells yields a powerful predictor of durable complete response *vs.* progression.

Discussion

Identification of biomarkers associated with response or toxicity following CAR T cell therapy could enable earlier interventions to improve outcomes and provide novel mechanistic insights into response and toxicity. Immunokinetic measurements of total CAR T cell levels in LBCL have been performed in numerous studies[2,6,8,15,47–52], and generally demonstrate inconsistent or weak correlations with response. In line with this, in 32 LBCL patients receiving commercial axi-cel at our institution, we observed that neither flow cytometric nor qPCR-based measurement of CAR T cell expansion associated with clinical response or long-term disease control (Fig. 1f, Fig. 6e, and Extended Data Fig. 1b-h). This could reflect the divergent mechanisms of resistance to CAR T cells[11], which include inadequate CAR T cell potency associated with low CAR T cell levels, but also intrinsic tumor resistance due to antigen-negative or antigen-low variants. Furthermore, efficient CAR T cell homing to the tumor may result in misleadingly low counts in blood, and patients with lower tumor burdens can experience disease control with relatively low levels of CAR T cell expansion in the peripheral blood.

We discovered that $CD4^+$ $CD57^-$ $Helios^+$ CAR T cells circulating at peak expansion (day 7) associate with progression at 6 months and milder neurotoxicity (Fig. 3b,e). Prospective analysis of the second cohort comprising 31 LBCL patients validated these associations (Fig. 6a,b) and identified an inverse correlation with CAR T cell expansion *in vivo* (Fig. 6d and Extended Data Fig. 9a). These cells are nearly exclusively $FOXP3^+$ $CD25^{High}$, polyclonal, and have a T_{Reg} gene expression program and low cytotoxic potential (Figs. 2g, 4, 5g, and Extended Data Figs. 2a, 8f), consistent with thymic-derived classical T_{Reg} cells[53], whose suppressive function would be expected to diminish antitumor response, toxicity, and expansion. Although we initially identified this population using Helios, quantification of CAR T_{Reg} based on FOXP3 led to nearly identical results (Fig. 6a,b). CAR T_{Reg} expansion *in vivo* was independent from the tumor burden quantified by LDH levels and synergistic with LDH as a predictor of response (Fig. 6f-i and Extended Data Fig. 10). Specific modulation of this subset in the graft or *in vivo* could provide a novel approach to either enhance antitumor effect or diminish neurotoxicity. Although we did not observe CAR T_{Reg} differences prior to infusion (Extended Data Fig. 5a), given the lack of access to axi-cel products, we could not determine whether expansion correlates with levels contained in the manufactured product. Future studies will examine the epigenetic state of the T_{Reg}-specific demethylated region (TSDR) within the *FOXP3* gene[54] and additional functional properties of this population.

The functional and phenotypic features of $CD57^+$ $T\text{-}bet^+$ CAR T cells described here (Figs. 2,4,5) are consistent with $CD57^+$ terminal effector T cells[55,56] in the early stages of senescence that remain highly cytolytic[34,38,57]. The senescence program may eventually

limit the longevity and renewal of these cells, leading to a rapid decline of circulating CAR T cell counts by week 4 post-infusion (Fig. 1d). In addition, higher expression of exhaustion marker CD101 in this subset or CD39 in $CD57^-$ cells were linked to progression (Extended Data Fig. 3). Helios could trigger an NK-cell transition program[46] in $CD57^+$ $T\text{-}bet^+$ subsets in patients who progress (Extended Data Fig. 9). However, this was not the case in our discovery cohort, and a CAR T cell cluster expressing CD57, T-bet, and Helios was observed in a CLL patient with a decade-long remission[58], indicating that biology of this subset still needs to be unraveled. Overall, our work highlights the importance of senescence and NK-cell transition, in addition to exhaustion, as potential sources of CAR T cell dysfunction.

Previous studies focused on the CAR T cell products have demonstrated that stemness features correlate with improved outcome[12,15], and CAR T cells in infusion products typically do not express CD57[35] (Extended Data Fig. 7b). We postulate that CAR T cells with high levels of fitness proliferate and differentiate into cytolytic $CD57^+$ $T\text{-}bet^+$ CAR T cells early following infusion, leading to a sustained malignant cell clearance, but accompanied by severe toxicity when peripheral CAR T cell expansion is high. However, polyclonal CAR T_{Reg} cells limit expansion, toxicity, and response. In addition, T_{EFF}-intrinsic exhaustion, senescence, and NK-cell transition may limit CAR T cell function. Here, CAR T cell efficacy still depends on tumor burden, adequate expression of the targeted antigen by the tumor, and effective CAR T cell trafficking and function within the tumor microenvironment. Indeed, although CAR T cell products are typically polyclonal[12,59], $CD57^+$ $T\text{-}bet^+$ CAR T cells demonstrated significant clonal restriction, consistent with a recent proliferative burst (Fig. 5h). Together, our data are consistent with CD57 marking clonally expanded CAR T cell populations, thereby providing a surrogate for CAR T cells that have undergone extensive proliferation *in vivo*.

In summary, despite the early successes of CAR T cell immunotherapies, many challenges remain to develop CAR T cells that induce durable and complete remissions in all cancer patients with acceptable toxicity. Our results highlight the power of deep single-cell correlative studies to interrogate the biology of a successful CAR T cell response and toxicity. Using this approach, we identified circulating CAR T_{Reg} cells as a novel biomarker of progression and reduced toxicity, and thus defined T cell characteristics that may be targets of manipulation in advanced therapies.

Methods

Patients

LBCL patients who received axi-cel as a standard-of-care treatment at the Stanford Hospital Center were eligible for this study. Patients provided informed consent for research using their blood samples and de-identified health information as a part of the Clinical Outcomes Biorepository protocol that was approved by the Institutional Review Board of Stanford University (IRB #43375). Clinical data were obtained retrospectively from the chart review (Supplementary Table S1). Treatment response was assessed radiographically according to the Lugano criteria[60], with date of progression defined as the date of radiographic

progression. Toxicity was evaluated by Lee criteria[61] for CRS and by ICANS grading[10] for neurotoxicity.

CAR T cell production

Where indicated, healthy donor T cells expressing the CD19-CD28ζ CAR were used as controls. As in axi-cel, the CD19-CD28ζ CAR contains the CD19-targeted FMC63 scFv, the transmembrane and intracellular domains of CD28, and the intracellular domain of CD3ζ. CAR T cells were produced as described previously[20]. Briefly, de-identified human buffy coats were obtained from healthy adult donors under informed consent according to an IRB-exempt protocol (Stanford Blood Center, Palo Alto, CA). T cells were isolated using the RosetteSep Human T Cell Enrichment kit (Stem Cell Technologies) according to the manufacturer's instructions using Lymphoprep density gradient medium and SepMate-50 tubes. For long-term storage, T cells were cryopreserved at 1–2×10^7 T cells per vial in 1 mL of CryoStor CS10 cryopreservation medium (Stem Cell Technologies) and stored in liquid nitrogen. The retroviral vector encoding CD19-CD28ζ CAR was described previously[62]. This vector was produced using the 293GP packaging cell line co-transfected with RD114 envelope plasmid and MSGV plasmid encoding the CD19-CD28ζ CAR using Lipofectamine 2000 (Thermo Fisher Scientific). Supernatant was collected at 48 and 72 hours after transfection, centrifuged to remove cell debris, and frozen at −80°C for future use. Cryopreserved T cells were thawed and activated same day with Human T-Expander CD3/CD28 Dynabeads (Gibco) at 3:1 beads:cell ratio in T cell medium containing AIMV (Gibco) supplemented with 5% heat-inactivated fetal bovine serum (FBS; Sigma-Aldrich), 10 mM HEPES (Gibco), 2 mM GlutaMAX (Gibco), 100 U/mL penicillin, and 100 μg/mL streptomycin (Gibco). Recombinant human IL-2 (Peprotech) was added at 100 U/mL. T cells were transduced with the retroviral vector on days 2 and 3, maintained in T cell medium with IL-2, and cryopreserved on days 11 or 12 after activation.

Flow cytometry assay to monitor CAR T cell expansion

Blood samples were collected pre-lymphodepletion, on day 0 (the day of axi-cel infusion), day 7 (± 2), day 14 (± 4), day 21 (± 4), and day 28 (± 4) post-infusion. Peripheral blood mononuclear cells (PBMCs) were isolated from 8 mL of fresh whole blood by density gradient centrifugation using Ficoll-Paque Plus (GE Healthcare, Chicago, IL, USA) according to manufacturer's instructions. PBMCs were stained with fixable Live/Dead Aqua amine-reactive viability stain (Invitrogen #L-34965). Fc receptors were blocked with Human TruStain FcX (Biolegend #422302) for 5 minutes to prevent non-specific antibody binding. Cells were then stained at room temperature with the fluorochrome-conjugated antibody panel (Supplementary Table S3). In-house CAR T cells were used as a positive control included in daily staining experiments. Stained and fixed cells were acquired on a four-laser LSRII flow cytometer (BD Biosciences; Blue: 488 nm, Violet: 405 nm, Red: 640nm, Green: 532 nm lasers; 21 parameters). At least 10^6 cells were acquired unless restricted by the number of cells isolated from blood. $CD4^+$ and $CD8^+$ CAR T cells were gated using *Cytobank* software as $CD3\varepsilon^+$ $CD4^+$ $CD8\alpha^-$ CAR^+ or $CD3\varepsilon^+$ $CD4^-$ $CD8\alpha^+$ CAR^+ events among single viable $CD45^+$ lymphocytes, as defined by the forward and side scatter gates. Absolute CAR T cell numbers were calculated by multiplying the percentages of CAR T cells among lymphocytes by the absolute lymphocyte count obtained on the same day. The

assay limit of detection (LOD) was calculated as 1 in 10^4 of total acquired PBMCs or 0.0125 cells/μL.

Quantitative PCR assay to monitor CAR T cell expansion

DNA was extracted from 2–5×10^6 PBMCs using QIAmp DNA Blood Mini Kit (Qiagen #51306). FMC63 sequence of the CD19-CD28ζ CAR and albumin control sequence were quantified by qPCR using the primer and probe sets listed in Supplementary Table S3. For the standard curve, a custom minigene plasmid was designed containing a partial CAR sequence and a partial albumin sequence, which served as a control for normalization. The standard curve contained a 10-fold serial dilution of plasmid between 5 and 5×10^6 copies. Both plasmid and patient DNA from each time point were run in triplicate, with mean of 3 replicates reported. Each reaction contained 5 μL (50 ng) DNA, 100 nM forward and reverse primers, and 150 nM probe resuspended in 10 μL TaqMan Fast Universal PCR Master Mix (2X), No AmpErase UNG or equivalent (Thermo Fisher Scientific), and 5 μL TE buffer (Invitrogen #AM9935). The Bio-Rad CFX96 Touch Real-Time PCR Detection System was used for qPCR with 20 μL per reaction. The quality metrics for all qPCR standard curve results were $R^2 > 0.99$, -3.38 > slope > -3.71, and efficiency > 90%. The assay LOD was calculated as 8 copies per 50 ng DNA reaction with 95% confidence.

CyTOF

PBMCs cryopreserved prior to axi-cel infusion (pre-lymphodepletion or on day 0), on day 7 (± 2), and on day 21 (± 4) were analyzed by CyTOF in batches of 18 samples (6 patients). Each batch also contained PBMCs from a healthy donor and in-house CAR T cells as controls. Samples were processed as previously described[29]. Briefly, cryopreserved PBMCs were thawed into 9 mL of cell culture medium (CCM; RPMI 1640 containing 10% FBS, 10 mM HEPES, 2 mM GlutaMAX, 100 U/mL penicillin, and 100 μg/mL streptomycin) supplemented with 25 U/mL benzonase (Sigma-Aldrich #E8263–5KU). Cells were then pelleted for 5 minutes at 300 *g*, resuspended in 10 mL CCM, filtered through a 70 μm strainer, and counted.

To stain cells for viability[63], cisplatin (Sigma-Aldrich #P4394) was reconstituted to 100 mM in DMSO and incubated at 37°C for 3 days to prepare a stock solution, which was then stored in aliquots at −20°C. Cell pellets were resuspended in 1 mL PBS containing 0.5 μM cisplatin, gently vortexed, incubated 5 minutes at room temperature, quenched with 3 mL CCM, pelleted, and resuspended in 1 mL CCM. Cells were fixed by adding 16% paraformaldehyde (PFA; Electron Microscopy Sciences, Hatfield, PA, USA) to a final concentration of 2%, gently vortexed, incubated 10 minutes at room temperature, and washed twice with cell staining media (CSM; PBS with 0.5% BSA, 0.02% sodium azide) to remove residual PFA. All centrifuging steps for fixed cells were done for 5 minutes at 600 *g*, 4°C. With the exception of antibody titrations, samples were palladium-barcoded and pooled as described[64] to improve staining consistency.

CyTOF antibody panels are listed in the Supplementary Table S3. With the exception of antibodies purchased from Fluidigm, all antibodies were conjugated to reporter metal isotopes in-house and titrated to determine optimal staining concentrations prior to

incorporating into a staining panel. Antibodies were conjugated using MaxPar Antibody Conjugation Kit (Fluidigm) and titrated on cells both positive and negative for the target antigen expression to identify concentration yielding the best signal-to-noise ratio. Fc receptor blocking was performed with Human TruStain FcX (Biolegend #422302) following manufacturer's instructions to prevent non-specific antibody binding. Antibodies against surface antigens were pooled into a master mix in CSM yielding 50 μL (350 μL if barcoded) final reaction volumes per sample and filtered through a 0.1 μm filter (Millipore #UFC30VV00, Billerica, MA, USA) for 5 minutes at 1,000 *g* to remove antibody aggregates. Antibody master mix was then added to each sample, resuspended, and cells were incubated 30 minutes at room temperature. Following the surface stain, cells were washed with CSM, permeabilized with 4°C methanol for 10 minutes on ice, washed twice with CSM, stained with an antibody master mix (prepared as above) against intracellular antigens in 50 μL (350 μL if barcoded) CSM for 30 minutes at room temperature, and washed once with CSM. To stain DNA, cells were incubated in PBS containing 1:5000 ^{191}Ir/^{193}Ir MaxPar Nucleic Acid Intercalator (Fluidigm) and 1.6% PFA for 1–3 days at 4°C. Just prior to analysis, cells were washed once with CSM and twice with filtered double-distilled water, resuspended in normalization beads[65] (EQ Beads, Fluidigm), filtered, and placed on ice. During event acquisition, cells were kept on ice and analyzed on the Helios mass cytometer (Fluidigm). In addition to reporter metal isotopes listed in antibody panels, we recorded event length, width, and channels ^{102}Pd, ^{104}Pd, ^{105}Pd, ^{106}Pd, ^{108}Pd, and ^{110}Pd (barcoding); ^{140}Ce, ^{151}Eu, ^{153}Eu, ^{165}Ho, and ^{175}Lu (bead normalization); ^{191}Ir and ^{193}Ir (DNA); ^{195}Pt and ^{196}Pt (dead cells); and ^{138}Ba (to help define single cells).

CyTOF data processing

CyTOF data were processed using *R* (www.r-project.org) and *Bioconductor* (www.bioconductor.org) software (Supplementary Table S3). Raw FCS files were bead normalized[65] using *premessa* and concatenated using *CATALYST*. Panels were harmonized, and samples were debarcoded[64] using *premessa*. Cells were gated using *Cytobank* software based on event length and ^{191}Ir/^{193}Ir (DNA) content[29]. Single live non-apoptotic cells were gated based on ^{195}Pt (viability)[63], cleaved PARP (cPARP) (apoptotic cells), and ^{138}Ba (single cells). Lymphocytes were selected based on CD45 expression. Next, data were transformed using inverse hyperbolic sine (asinh) with a cofactor of 5 (and cofactor of 30 for CD4 and CD57) using *flowCore*[66] and *ncdfFlow*. Batch normalization was performed using *cydar*[32]. T cells were gated as CD4$^+$ or CD8α$^+$ events, and CAR$^+$ and CAR$^-$ T cells were selected based on CAR expression using *Cytobank*.

Circulating CAR T cells on day 7 post-infusion were organized with self-organizing maps (SOMs) into 25 clusters, connected into a minimum spanning tree (MST), and grouped into 10 metaclusters using *FlowSOM*[67] implementation in *Cytobank*. Differentiation abundance analysis was performed using *cydar*[32] on CAR T cells in blood on day 7 that were subsampled to 400 cells per patient.

CAR T cell functional assay

PBMCs cryopreserved on day 7 following axi-cel infusion were thawed and counted (as in CyTOF section). Up to 2×10^6 live cells were stimulated with 5 ng/mL phorbol 12-myristate

13-acetate (PMA; Sigma-Aldrich #P1585) and 500 ng/mL ionomycin (Sigma-Aldrich #I0634). To stimulate CAR T cells through CAR, a flat-bottom non-TC-treated 96-well plate (Falcon #351172) was coated with 5 μg/mL anti-FMC63 scFv idiotype antibody[27] in 100 μL PBS (Gibco) for 16 hours at 4°C. Just before seeding the cells, coated wells were washed twice with 200 μL PBS and immediately seeded with 300,000 live cells. All test wells contained 1x monensin (Thermo Fisher Scientific #00–4505-51), one test of CD107a-BV785 antibody (Supplementary Table S3) and filled to 200 μL with CCM. All samples were analyzed in one batch. Healthy donor T cells and in-house CAR T cells were included as controls. Once the assay was setup, the 96-well plate was centrifuged at 200 *g* for 3 minutes and incubated at 37°C for 6 hours. Cells were then transferred into a 96-well V-bottom plate (Corning #3894) and analyzed by intracellular flow cytometry (see below).

Intracellular flow cytometry assay

Following CAR T cell functional assay, cells were stained with Fixable Viability Stain 780 (BD #565388) for 5 minutes at room temperature. For the validation cohort analysis, we stained day 7 thawed and counted cryopreserved PBMCs with Fixable Aqua Dead Cell Stain Kit (Thermo Fisher Scientific #L34957). Fc receptors were blocked with Human Fc block (BD #564220) in FACS buffer (PBS with 2% FBS). Next, cells were stained with surface and intracellular antibody master mixes (Supplementary Table S3) using Foxp3 / Transcription Factor Staining Buffer Set (eBioscience #00–5523-00) following manufacturer's instructions. Finally, cells were resuspended in 200 μL FACS buffer and analyzed on LSRFortessa flow cytometer (BD Biosciences; for CAR T cell functional assay) or five-laser LSRII flow cytometer (BD Biosciences; for validation cohort analysis). Data were analyzed using *Cytobank* software. For the CAR T cell functional assay, single live $CD4^+$ and $CD4^-$ CAR T cells were gated as $CD19^-$ $CD33^-$ CAR^+ events among single viable lymphocytes, as defined by the forward and side scatter gates. For the validation cohort analysis, we gated $CD3\varepsilon^+$ $CD4^+$ $CD8\alpha^-$ CAR^+ or $CD3\varepsilon^+$ $CD4^-$ $CD8\alpha^+$ CAR^+ events among single viable $CD14^-$ $CD19^-$ $CD33^-$ $CD45^+$ lymphocytes, as defined by the forward and side scatter gates. Due to considerable sample degradation and paucity of cells in the validation cohort, we only reported values for $CD4^+$ and $CD8^+$ CAR T cell populations with ≥100 cells detected. When analyzing $Helios^+$ cells within a rare $CD57^+$ $T\text{-}bet^+$ population, we reported values for all patients with ≥10 $CD4^+$ or $CD8^+$ $CD57^+$ $T\text{-}bet^+$ CAR T cells detected.

Single-cell sequencing

5' single-cell sequencing of whole transcriptome (scRNA-seq), αβTCR (scTCR-seq), and cell surface epitope expression (CITE-seq) of sorted CAR T cells was performed using the 5' Immune Profiling with Feature Barcoding technology (10X Genomics) according to the manufacturer's protocol. Briefly, fresh PBMCs were obtained on day 7 following axi-cel infusion, resuspended in PBS with 0.2% BSA, and stained with Human TruStain FcX (Biolegend #422302), LIVE/DEAD Fixable Blue Dead Cell Stain Kit (Thermo Fisher Scientific #L34962), antibodies for fluorescence-activated cell sorting (FACS) (Supplementary Table S3), and CITE-seq antibodies (Supplementary Table S3) in presence of 1% dextran sulfate sodium salt (Thermo Fisher Scientific #AC441490050) to prevent oligo-labeled antibody aggregation. Next, 50,000–70,000 CAR T cells (single

live $CD4^+$ or $CD8\alpha^+$ $CD235a^-$ CAR^+ events) were sorted on FACSAria Fusion cell sorter (BD Biosciences) to ≥95% purity. Debris was excluded by adjusting the threshold setting and applying a scatter gate during FACS. Sorted CAR T cells were counted, resuspended to 700–1,200 cells/μL, and captured using Single Cell Chip A on the 10X Chromium Controller (10X Genomics) to generate Gel Bead-In Emulsions (GEMs). Reverse transcription inside GEMs was performed using a C1000 Touch Thermal Cycler (Bio-Rad). Barcoded complementary DNA (cDNA) was recovered through post-GEM-RT cleanup and PCR amplification. Recovered cDNA was amplified and used to construct 5' whole transcriptome, αβTCR, and cell surface epitope libraries. Quality of cDNA and each library was assessed using Agilent 2100 Bioanalyzer. The libraries were indexed using a Chromium i7 Sample Index Kit, pooled, and sequenced on HiSeq 4000 or NovaSeq 6000 Systems (Illumina).

Singe-cell sequencing data processing

Raw single-cell sequencing data were processed using the *Cell Ranger* software (10X Genomics). Sequencer's base call files (BCLs) were demultiplexed into FASTQ files using the *cellranger mkfastq* pipeline. FASTQ reads for scRNA-seq and CITE-seq were aligned to the GRCh38 human genome reference (for scRNA-seq) and to a custom Feature Barcode reference (for CITE-seq) using the *cellranger count* pipeline. FASTQ reads for scTCR-seq were aligned to the vdj-GRCh38 reference using the *cellranger vdj* pipeline.

Unique molecular identifier (UMI) count matrices from *Cell Ranger* were analyzed using *Seurat*[37,68]. Clonotype data was included into the metadata for each sample. Dead cells and cell debris with >15% of UMI counts mapping to mitochondrial genes or <300 genes detected were excluded from the analysis. Cell doublets containing >10,000 genes or >100,000 UMI counts were also excluded. Next, scRNA-seq data were normalized by the sequencing depth using the *SCTransform* pipeline[69] using a single model for all samples. CITE-seq data were first normalized using centered log ratio (CLR) transformation with unsatisfactory results. We therefore normalized CITE-seq data by the sequencing depth for all samples together using *SCTransform*, followed by asinh transformation of SCT count data with custom factors for each marker. We predicted surface protein expression for the missing CD8α CITE-seq antibody in CAR T cells from patient 116 (Supplementary Table S3). To do this, we built a weighted nearest neighbor (WNN) embedding reference, and a mapping between the scRNA-seq and CITE-seq data[37], using the data from all patients except 116 with *FindMultiModalNeighbors*, *RunSPCA*, *FindNeighbors*, and *FindTransferAnchors*. We then predicted CITE-seq data for patient 116 by projecting its scRNA-seq data using *MapQuery* and the above reference using the transfer anchors calculated above. We only used predicted CITE-seq data for surface CD8α and used measured CITE-seq for all other surface epitopes for patient 116.

Principal component analysis (PCA) of normalized scRNA-seq data was performed using all 2,000 variable genes with the exception of TCR and BCR genes to prevent clonotypes from driving the final layout, as well as sex-associated genes (*XIST*, *RPS4Y1*, *RPS4Y2*) and mitochondrial genes (*MT-**). In addition, a set of curated genes relevant to T cell function or cell type identification were included into the list of variable genes. PCA of

normalized CITE-seq data was performed using all measured T cell epitopes. WNN-based UMAP embedding (wnnUMAP) was constructed using the first 30 principal components from scRNA-seq data and the first 10 principal components from CITE-seq data. Cell cycle score and stage were assigned to each cell using the *CellCycleScoring* pipeline based on 97 canonical cell cycle markers[45]. Cell subsets and expression of additional CITE-seq markers were identified by projecting data onto an annotated reference dataset using *Azimuth*[37]. We only included predicted expression of surface CTLA4 in Extended Data Fig. 8f and did not use other predicted values. Cell population identities were assigned as shown in Fig. 5b to all cells following removal of non-T cells and aggregates of CAR T cells bound to myeloid cells. Differential expression analysis was performed using the *FindMarkers* pipeline for all genes expressed in ≥5% cells, with *EnhancedVolcano* used to visualize results in a volcano plot. Pathway enrichment analysis was performed on results from differential expression analysis using *Reactome*[70].

Statistical analysis

Statistical analysis was performed using *R* statistical software (www.r-project.org). Data were summarized using *dplyr* and plotted with either *ggplot2* or *ComplexHeatmap*[71]. To test for statistical significance in 2x2 tables, we used two-sided Fisher's exact test in *exact2x2*. To test association of two factors with more than two levels, we used general Cochran-Mantel-Haenszel chi-squared test in *vcdExtra*. We applied unpaired two-sided Wilcoxon-Mann-Whitney *U* test to assess statistical significance between two groups of unpaired samples. When more than two groups were compared, we first used Kruskal-Wallis *H* test (one-way analysis of variance on ranks) to check whether there are differences among treatment groups, followed by unpaired two-sided Wilcoxon-Mann Whitney *U* test applied to each treatment pair, and Bonferroni correction to correct for multiple hypothesis testing. If samples were paired, we used Friedman test, followed by pairwise two-sided Wilcoxon signed-rank tests and Bonferroni correction to adjust for multiple hypothesis testing. To assess correlation, we calculated either Spearman's rank correlation coefficient or Pearson correlation coefficient, as indicated, and a *P*-value using the correlation test. Radar plots were built using *fmsb*.

Area under the curve (AUC) and area under the moment curve (AUMC) were calculated using *pkr*[72] on days 0 (no CAR T cells), 7, 14, 21, and 28. $AUC_{0–28}$, $AUMC_{0–28}$, and peak CAR T cell expansion were calculated only when data were obtained for at least two timepoints.

Overall survival (OS), progression-free survival (PFS), and time to progression (TTP) were estimated with the Kaplan-Meier (KM) method using *survival* and *GGally* in R. OS was determined from the date of infusion to the date of death or the last follow-up. TTP was calculated from the date of infusion to the date of progression or the last follow-up. PFS was computed from the date of infusion to the date of progression, death, or the last follow-up, with both progression and death scored as an event. Due to an increased rate of death unrelated to progression during the global pandemic, we present data as TTP, except for Fig. 1b, where comparison to PFS in a prior study is made.

To construct a lasso logistic regression ("binomial") model, we used *glmnet*[73] with α = 1 and 10-fold cross-validation to tune the L_1 regularization parameter λ. Metaclusters 2 (cell doublets) and 10 (cell fragments) were excluded prior to the model construction. To fit a logistic regression model, we applied *glm* function in R to the discovery cohort data. We plotted the receiver operating characteristic (ROC) curve and determined the optimal probability threshold using *InformationValue* on the discovery cohort data. Variable importance in each model was assessed using *caret*[74]. Variance inflation factor (VIF) to assess multicollinearity was calculated using *car*. The model with the selected threshold was then applied to the validation cohort to assess performance on unseen samples, including sensitivity, specificity, and the misclassification error rate.

Figures were created with *Illustrator* (Adobe) and *BioRender* (https://biorender.com).

Extended Data

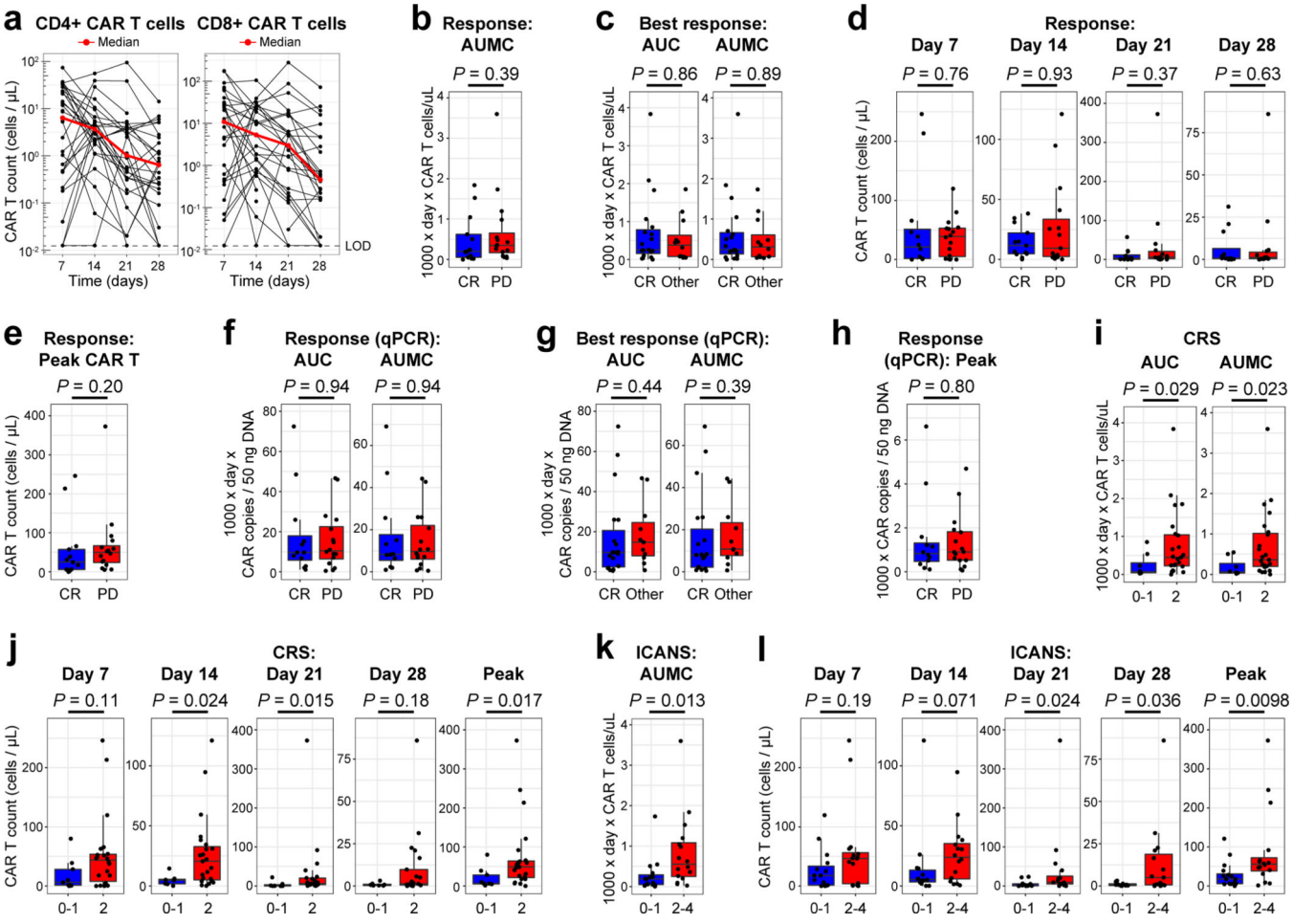

Extended Data Fig. 1. Peripheral CAR T cell expansion is associated with toxicity and not with clinical response at 6 months.

a, Absolute counts of $CD4^+$ (*left*) and $CD8^+$ (*right*) CAR T cells in blood on days 7, 14, 21, and 28 following axi-cel infusion (n = 32 patients, 128 observations). LOD, limit of detection. **b**, CAR T cell $AUMC_{0–28}$ for patients in CR or PD at 6 months (n = 29;

patients 042 and 058 had PR and SD at 6 months, respectively; patient 032 died from a non-progression related cause prior to 6 months). **c**, CAR T cell $AUC_{0–28}$ (*left*) and $AUMC_{0–28}$ (*right*) stratified by the best response as CR or other (PR, n = 9; SD, n = 1; PD, n = 2; no data for patient 058) (n = 31). **d**, Absolute CAR T cell counts in blood on days 7, 14, 21, and 28 for patients in CR or PD at 6 months (n = 28 on day 7, n = 28 on day 14, n = 26 on day 21, n = 26 on day 28). **e**, Absolute counts of circulating CAR T cells at peak expansion for patients in CR or PD at 6 months (n = 29). **f**, Quantitative PCR (qPCR) measuring CAR copies per 50 ng DNA in blood over 28 days as CAR T $AUC_{0–28}$ (*left*) and $AUMC_{0–28}$ (*right*) stratified for patients in CR or PD at 6 months (n = 28). **g**, qPCR CAR T $AUC_{0–28}$ (*left*) and $AUMC_{0–28}$ (*right*) stratified by the best response at 6 months as CR or other (PR, SD, PD) (n = 30). **h**, qPCR CAR copies per 50 ng DNA in blood at peak expansion for patients in CR or PD at 6 months (n = 28). **i**, CAR T cell $AUC_{0–28}$ (*left*) and $AUMC_{0–28}$ (*right*) stratified by maximum CRS grade (n = 31). **j**, Absolute CAR T cell counts in blood at peak expansion (n = 32) and on days 7 (n = 31), 14 (n = 30), 21 (n = 28), and 28 (n = 28) stratified by maximum CRS grade. **k**, CAR T cell $AUMC_{0–28}$ stratified by maximum ICANS grade (n = 31). **l**, Absolute CAR T cell counts in blood at peak expansion (n = 32) and on days 7 (n = 31), 14 (n = 30), 21 (n = 28), and 28 (n = 28) stratified by maximum ICANS grade. Boxplots in (b-l) show quartiles with a band at median, whiskers indicating 1.5 IQR, and all observations overlaid as dots. *P*-values are from two-sided Mann-Whitney *U* test.

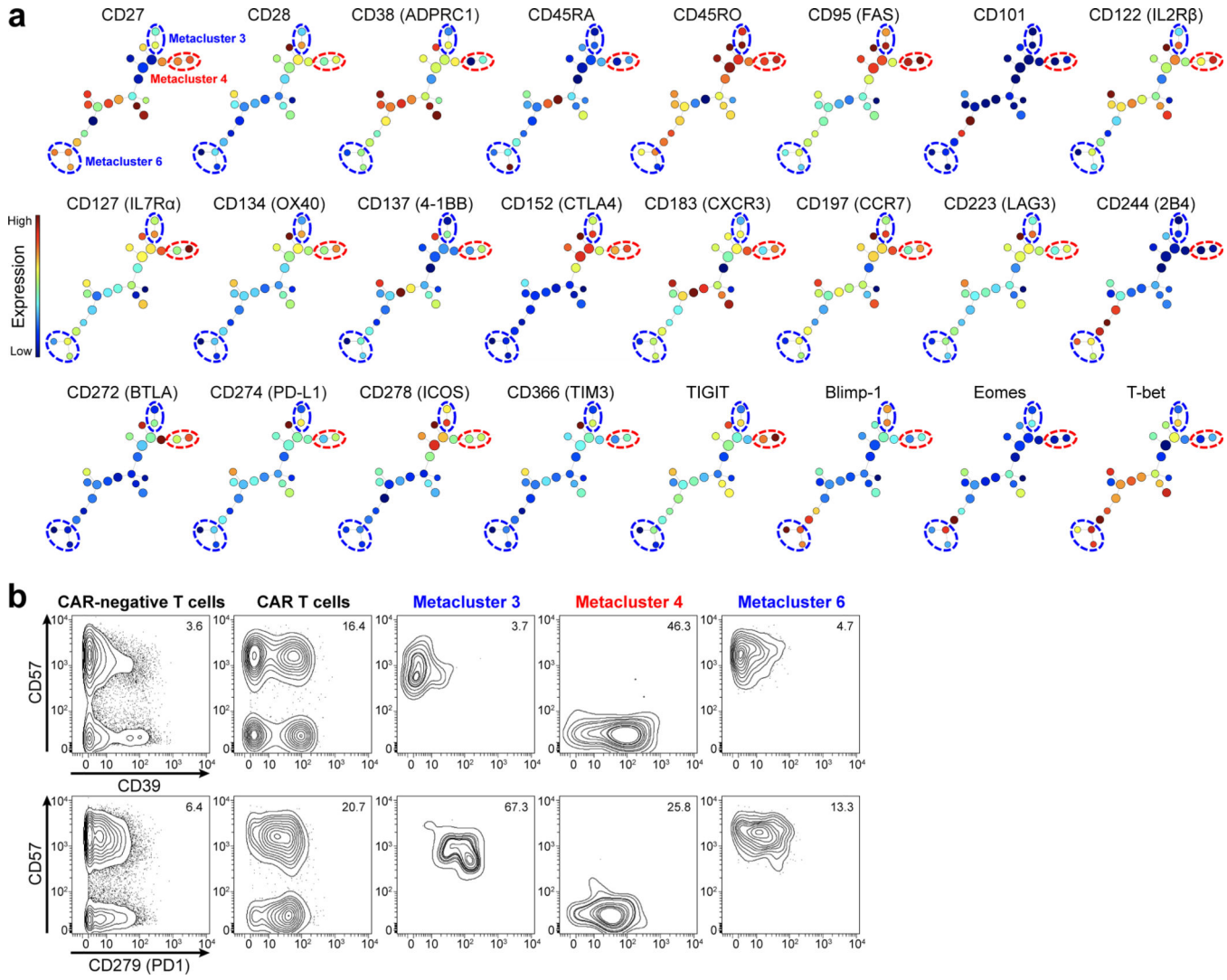

Extended Data Fig. 2. Protein expression in CyTOF metaclusters of circulating CAR T cells on day 7.

a, Expression of 24 proteins overlaid onto the minimum spanning tree from Fig. 2c, which shows hierarchical consensus clustering of circulating CAR$^+$ T cells on day 7 following axi-cel infusion (n = 31 patients), with 25 clusters grouped into 10 metaclusters. No CyTOF data were obtained for patient 038. Expressions of CD45 and CAR are not shown, as these proteins were used for gating and were not used for clustering. See Fig. 2g for the expression of the remaining proteins. **b**, Contour plots showing expression of exhaustion markers CD39 and CD279 (PD1) against senescence marker CD57 in CAR$^-$ and CAR$^+$ T cells, as well as in CAR T cell metaclusters 3, 4, and 6, for patient 004. Geometric mean for each marker on the X-axis is indicated in the top right corner of each plot.

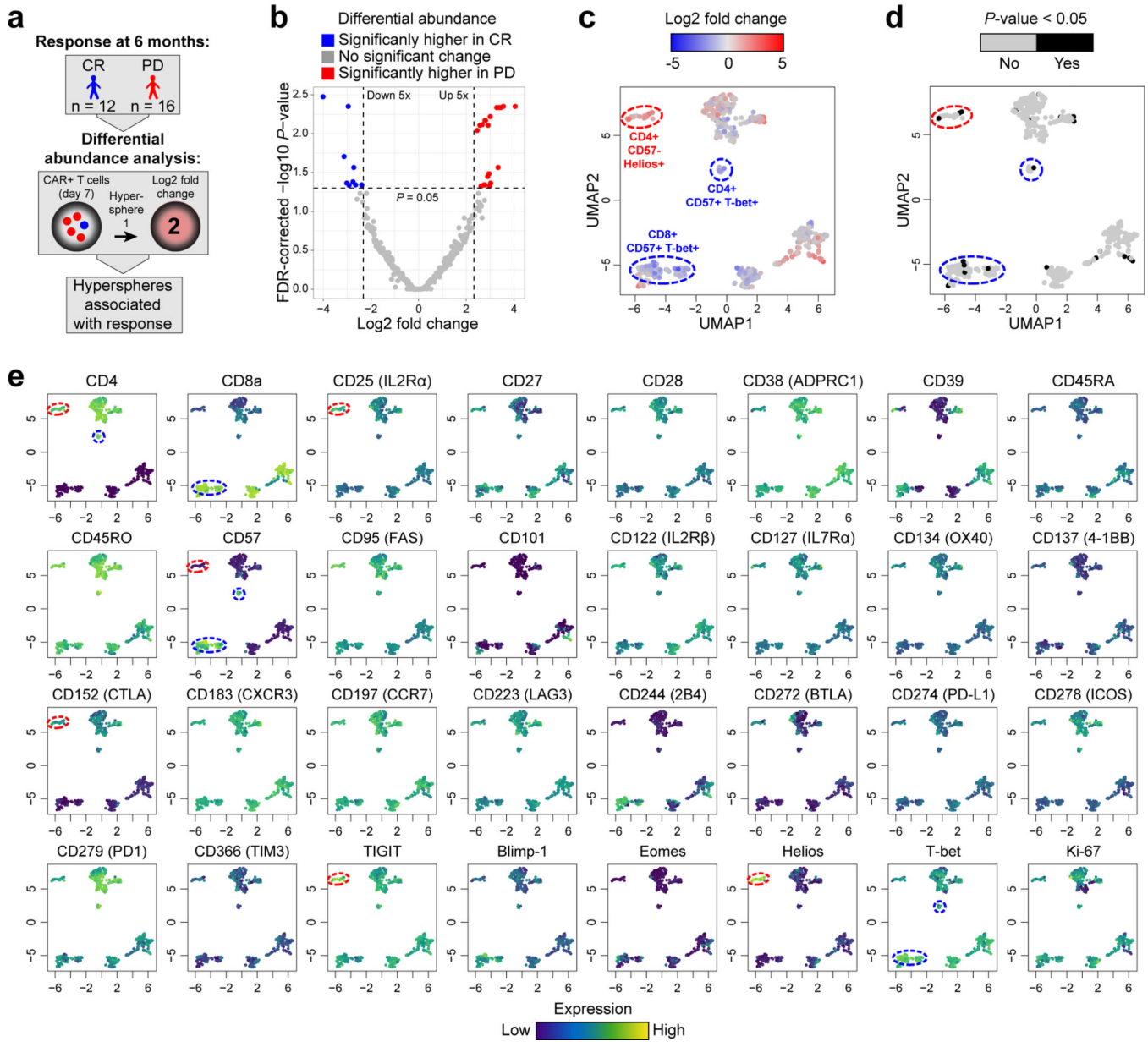

Extended Data Fig. 3. CAR T cell hyperspheres associated with clinical response at 6 months.

a, Schematic for differential abundance analysis comparing circulating CAR T cells on day 7 between patients in CR or PD at 6 months following axi-cel infusion (n = 28). CAR T cells falling into the same region of space in all dimensions (hypersphere) were quantified to generate comparison metrics for patients in CR *vs.* PD at 6 months. **b**, Volcano plot showing hyperspheres generated as described in (a) that are significantly differentially abundant between patients in CR or PD at 6 months. **c**, Log2 fold change overlaid onto hyperspheres from (a) that were embedded into UMAP coordinates. Groups of hyperspheres that correspond to the 3 CAR T cell populations identified by the lasso model in Fig. 2d are highlighted. **d**, FDR-corrected *P*-values overlaid onto hyperspheres from (c) and stratified

by the statistical significance threshold of $P < 0.05$. **e**, Individual marker expression overlaid onto hyperspheres from (c).

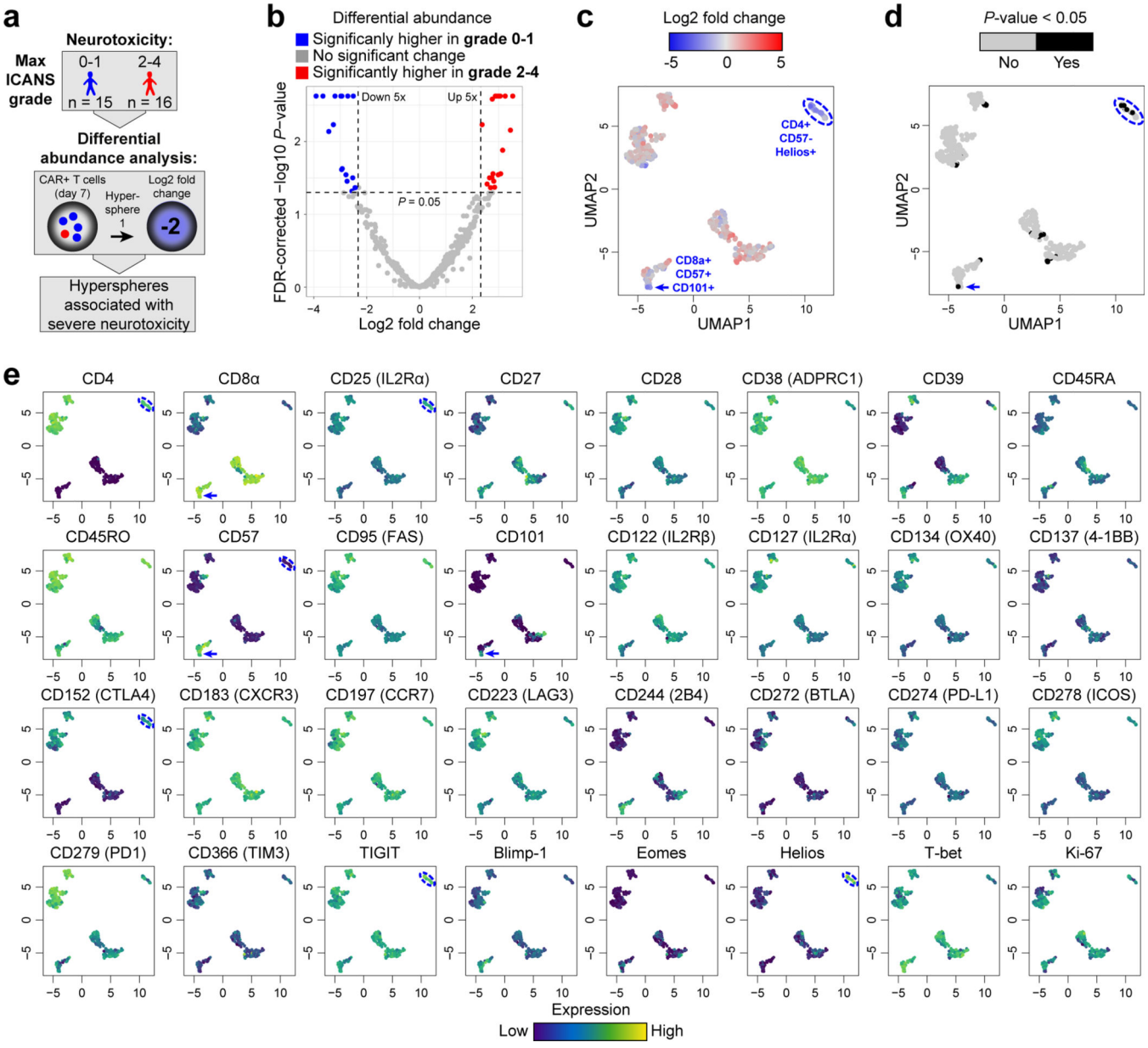

Extended Data Fig. 4. CAR T cell hyperspheres associated with severe neurotoxicity.

a, Schematic for differential abundance analysis comparing circulating CAR T cells on day 7 between patients with low (max ICANS grade 0–1) or severe (max ICANS grade 2–4) neurotoxicity (n = 31). CAR T cells falling into the same region of space in all dimensions (hypersphere) were quantified to generate comparison metrics for patients with low or severe neurotoxicity. **b**, Volcano plot showing hyperspheres generated as described in (a) that are significantly differentially abundant between patients with low (max ICANS grade 0–1) or severe (max ICANS grade 2–4) neurotoxicity. **c**, Log2 fold change overlaid onto hyperspheres from (b) that were embedded into UMAP coordinates. Groups of hyperspheres

that correspond to the 2 CAR T cell populations identified by the lasso model in Fig. 2h are highlighted. **d**, FDR-corrected *P*-values overlaid onto hyperspheres from (c) and stratified by the statistical significance threshold of $P < 0.05$. **e**, Individual marker expression overlaid onto hyperspheres from (c).

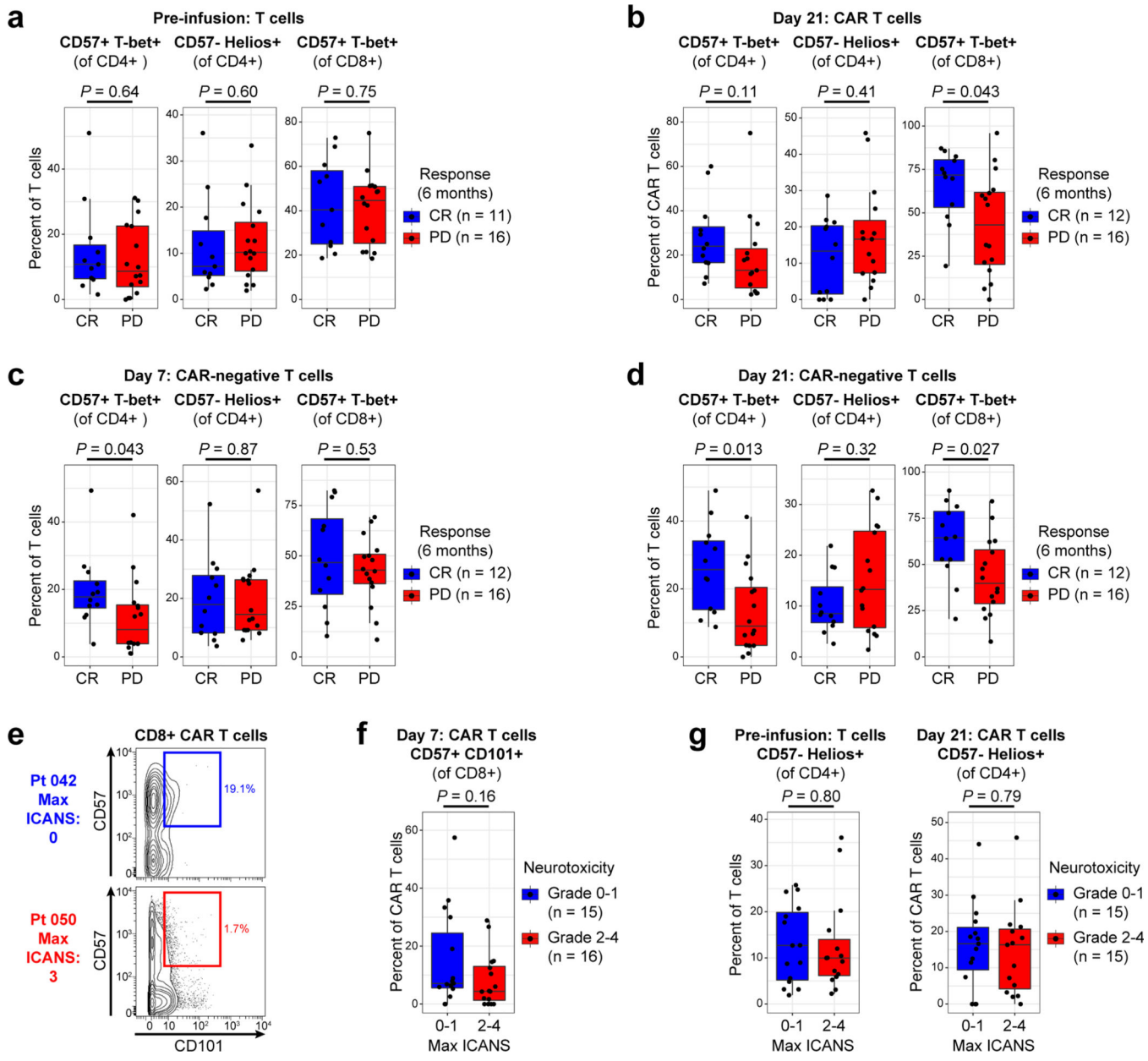

Extended Data Fig. 5. Dynamics of CAR T cell populations associated with clinical response or neurotoxicity.

a, Percentage of circulating T cells in 3 gates based on CyTOF data, as defined in Fig. 3a, prior to axi-cel infusion for patients in CR or PD at 6 months (n = 27; no pre-infusion sample for patient 005). **b**, Percentage of circulating CAR T cells on day 21 in 3 gates for patients in CR or PD at 6 months (n = 28; n = 27 for $CD4^+$ populations: n.d. for patient

040). **c-d**, Percentage of circulating CAR-negative T cells in 3 gates on day 7 (c) or day 21 (d) for patients in CR or PD at 6 months (n = 28). **e**, Gate defined based on metacluster 8 from the lasso model for predicting maximum ICANS grade as 0–1 *vs.* 2–4 based on metacluster abundance of circulating CAR T cells on day 7 (Fig. 2j). Contour plots show CyTOF data for CAR^+ T cells on day 7 from patients 042 (max ICANS grade 0) and 050 (max ICANS grade 3). **f**, Percentage of circulating $CD57^+$ $CD101^+$ cells among $CD8^+$ CAR T cells on day 7 in gate from (e) for patients with maximum ICANS grade 0–1 or 2–4 (n = 31). **g**, Percentage of $CD57^-$ $Helios^+$ cells among $CD4^+$ T cells in blood prior to axi-cel infusion (*left*; n = 30) or among $CD4^+$ CAR T cells on day 21 post-infusion (*right*; n = 30) for patients with maximum ICANS grade 0–1 or 2–4. Boxplots in (a-d,f,g) show quartiles with a band at median, whiskers indicating 1.5 IQR, and all observations overlaid as dots. *P*-values are from two-sided Mann-Whitney *U* test.

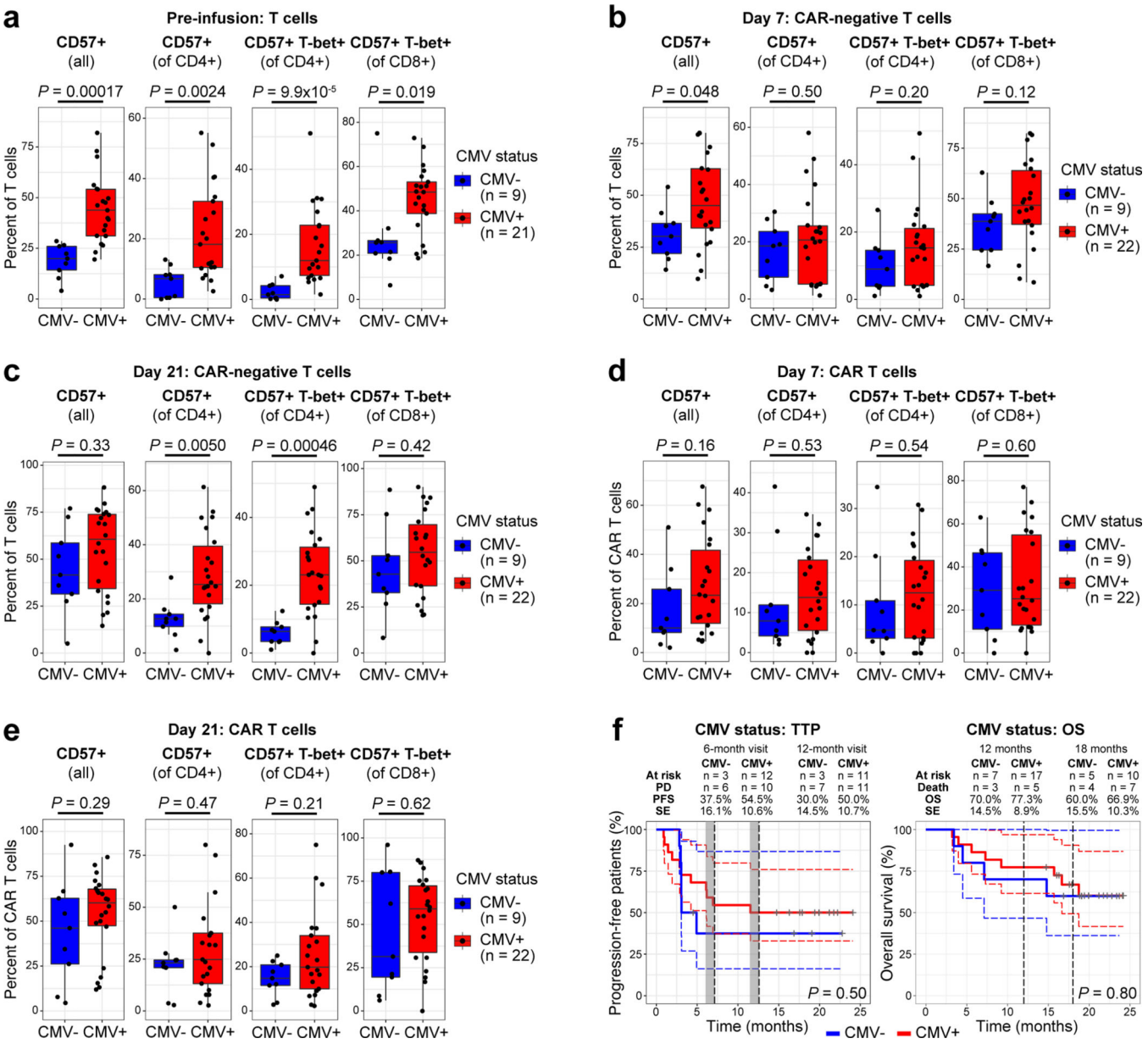

Extended Data Fig. 6. CMV status is not associated with prevalence of CD57-expressing CAR T cell populations or patient outcome.

a, Percentage of circulating $CD57^+$, $CD4^+$ $CD57^+$, $CD4^+$ $CD57^+$ T-bet^+, and $CD8^+$ $CD57^+$ T-bet^+ T cells based on CyTOF data prior to axi-cel infusion stratified by patient cytomegalovirus (CMV) infection status (n = 30). **b-e**, Percentage of circulating $CD57^+$ populations of CAR-negative (b-c) or CAR-positive (d-e) T cells on day 7 (b,d) or day 21 (c,e) stratified by patient CMV status (n = 31; n = 30 for $CD4^+$ CAR^+ T cells on day 21). **f**, Kaplan-Meier analysis of time to progression (TTP; *left*) and overall survival (OS; *right*) stratified by patient CMV status. Boxplots in (a-e) show quartiles with a band at median, whiskers indicating 1.5 IQR, and all observations overlaid as dots. *P*-values are from two-sided Mann-Whitney *U* test.

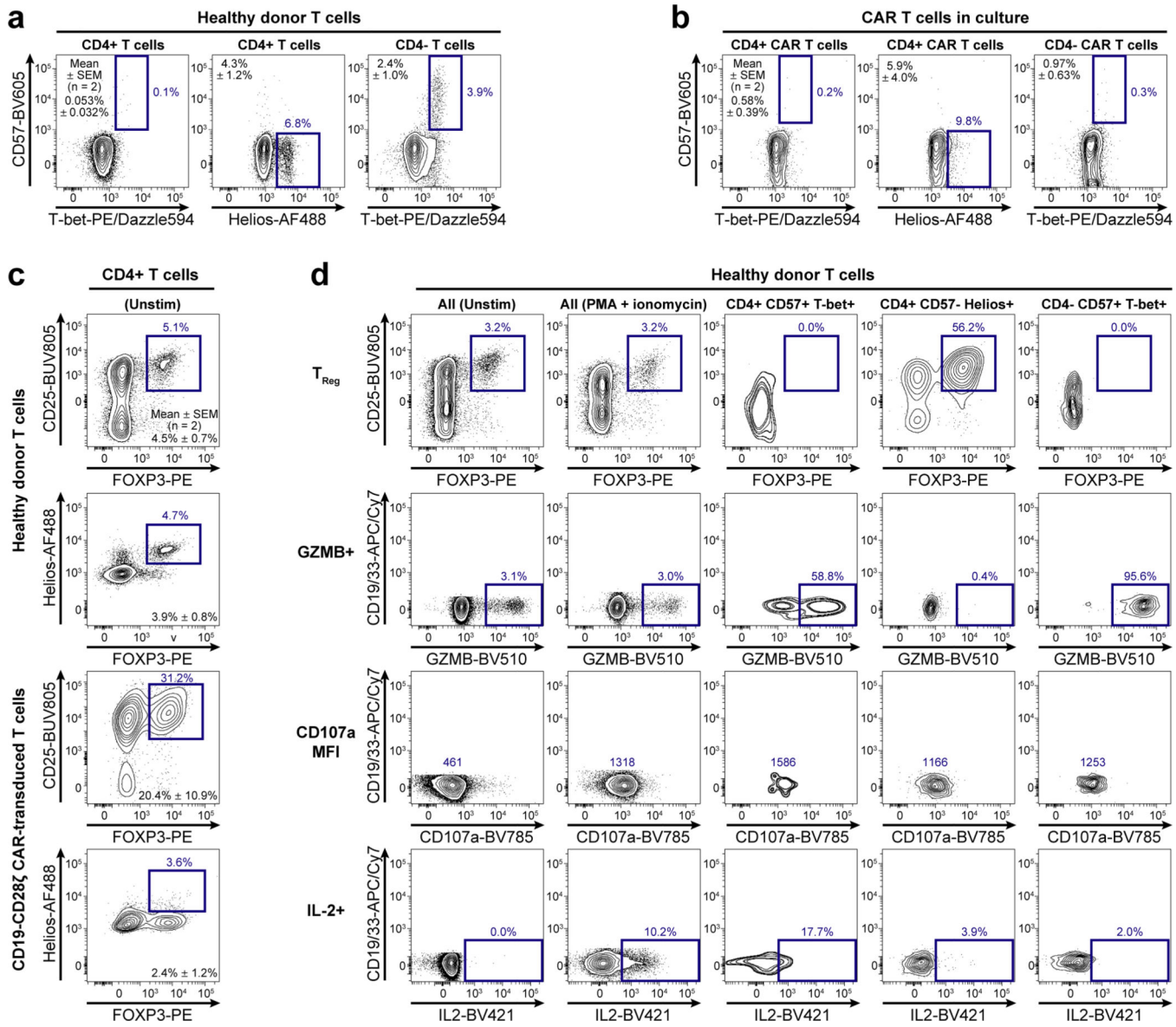

Extended Data Fig. 7. Identified populations in healthy donors and CD19-CD28ζ CAR-transduced T cells.

a-b, Contour plots show three identified populations among T cells from a healthy donor (a) and among CD19-CD28ζ CAR-transduced T cells generated in the lab (b). Population statistics for two donors are shown as mean ± SEM on each plot. **c**, Percentage of FOXP3^{+} CD25^{High} and FOXP3^{+} Helios^{+} cells among CD4^{+} T cells are shown for a healthy donor (*top*) and for CD19-CD28ζ CAR-transduced T cells generated in the lab (*bottom*). Population statistics for two donors are shown as mean ± SEM on each plot. **d**, Cryopreserved T cells from a healthy donor were incubated with PMA and ionomycin for 6 hours and analyzed by flow cytometry. Contour plots show gating strategy that was applied to patient samples in Fig. 4.

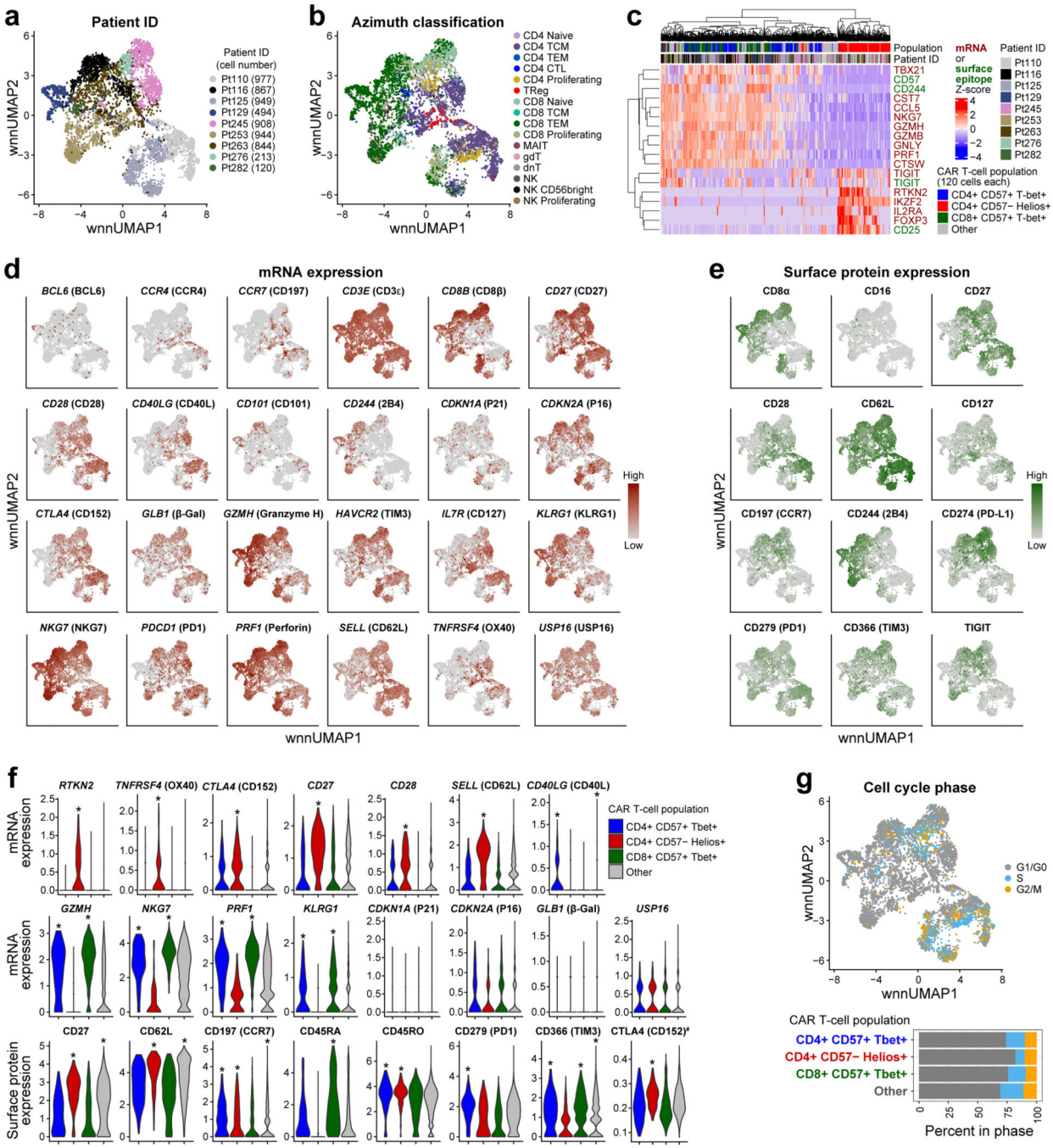

Extended Data Fig. 8. Selected gene and surface protein expression in three identified CAR T cell populations.

a, CAR^+ T cells were sorted from 9 LBCL patients on day 7 following axi-cel infusion and analyzed by scRNA-seq, scTCR-seq, and CITE-seq on the 10X Genomics platform. Patient IDs overlaid onto the wnnUMAP coordinates that integrate scRNA-seq and CITE-seq data (n = 6,316 cells). Numbers of filtered cells analyzed for each patient are indicated in parentheses. **b**, Cell subsets, which were defined by projecting data onto the public reference dataset containing leukocytes from healthy donors using *Azimuth*, overlaid onto

the wnnUMAP coordinates from (a). **c**, Heatmap showing distribution of selected mRNA and surface epitope markers of T_{Reg} and T_{EFF} subsets across patients in 120 cells sampled from each CAR T cell populations defined in Fig. 5b (n = 480 cells). **d**, Expression of selected genes overlaid onto the wnnUMAP coordinates from (a). Protein encoded by each gene is shown in parentheses. **e**, Surface expression of selected proteins overlaid onto the wnnUMAP coordinates from (a). **f**, Violin plots showing selected gene and surface protein expression across CAR T cell populations defined in Fig. 5b (n = 6,316 cells). Stars denote significant ($P < 0.05$) upregulation in the indicated population relative to all populations without stars. Other significant relationships are not denoted. *P*-values were calculated using Kruskal-Wallis *H* test, followed by unpaired two-sided Wilcoxon-Mann Whitney *U* test applied to each treatment pair, with Bonferroni correction for multiple hypothesis testing. #CD152 surface expression was predicted using *Azimuth*. **g**, Cell cycle phases overlaid onto the wnnUMAP coordinates from (a) (*top*) and shown as a bar plot in each CAR T cell population (*bottom*).

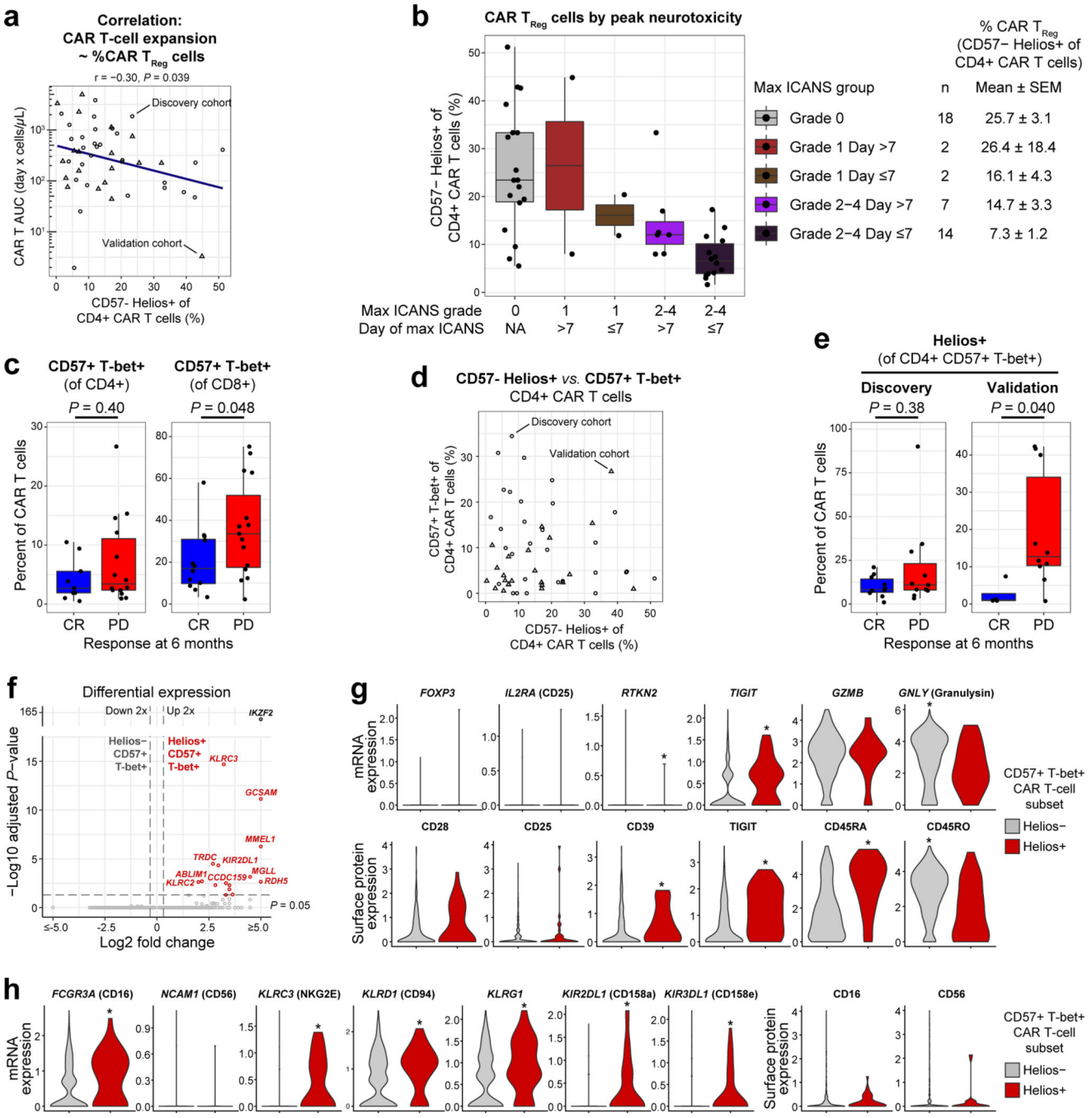

Extended Data Fig. 9. Helios-expressing CD57$^+$ T-bet$^+$ CAR T cells display an NK-like transition program.

a, Pearson correlation between percentage of CD57$^-$ Helios$^+$ cells among CD4$^+$ CAR T cells and expansion of CAR T cells, quantified as log10 $AUC_{0–28}$ for all study patients with available data (n = 49). *P*-value is from the correlation test. **b**, Percentage of CD57$^-$ Helios$^+$ cells among CD4$^+$ CAR T cells separated by maximum ICANS grade and day of maximum ICANS (n = 54). **c**, Percentage of CD57$^+$ T-bet$^+$ cells among CD4$^+$ CAR T cells (*left*, n = 23) or CD8$^+$ CAR T cells (*right*, n = 27) in blood on day 7 post-infusion separated

by response at 6 months in patients from the validation cohort with ≥100 $CD4^+$ or $CD8^+$ CAR T cells detected, respectively. **d**, Scatter plot showing percentage of $CD57^-$ $Helios^+$ *vs.* $CD57^+$ $T\text{-}bet^+$ cells among $CD4^+$ CAR T cells in both discovery and validation cohorts (n = 54). **e**, Percentage of $Helios^+$ cells among $CD4^+$ $CD57^+$ $T\text{-}bet^+$ cells separated by response at 6 months in patients from the discovery (*left*, n = 21) or validation (*right*, n = 19) cohorts with ≥10 $CD4^+$ $CD57^+$ $T\text{-}bet^+$ CAR T cells detected. **f**, Volcano plot showing differentially expressed genes comparing $Helios^+$ to $Helios^-$ cells within $CD57^+$ $T\text{-}bet^+$ CAR T cells (n = 774 cells) using scRNA-seq data from 9 LBCL patients on day 7 following axi-cel infusion. Differentially upregulated genes are in red; genes used to define each population are in black. **g-h**, Violin plots showing selected T cell (b) or NK-related (h) gene and surface protein expression in $Helios^-$ and $Helios^+$ cells within $CD57^+$ $T\text{-}bet^+$ CAR T cells (n = 774 cells). Stars denote significant ($P < 0.05$) upregulation in the indicated population relative to the population without a star. Boxplots in (b,c,e) show quartiles with a band at median, whiskers indicating 1.5 IQR, and all observations overlaid as dots. *P*-values were calculated using two-sided Wilcoxon-Mann Whitney *U* test.

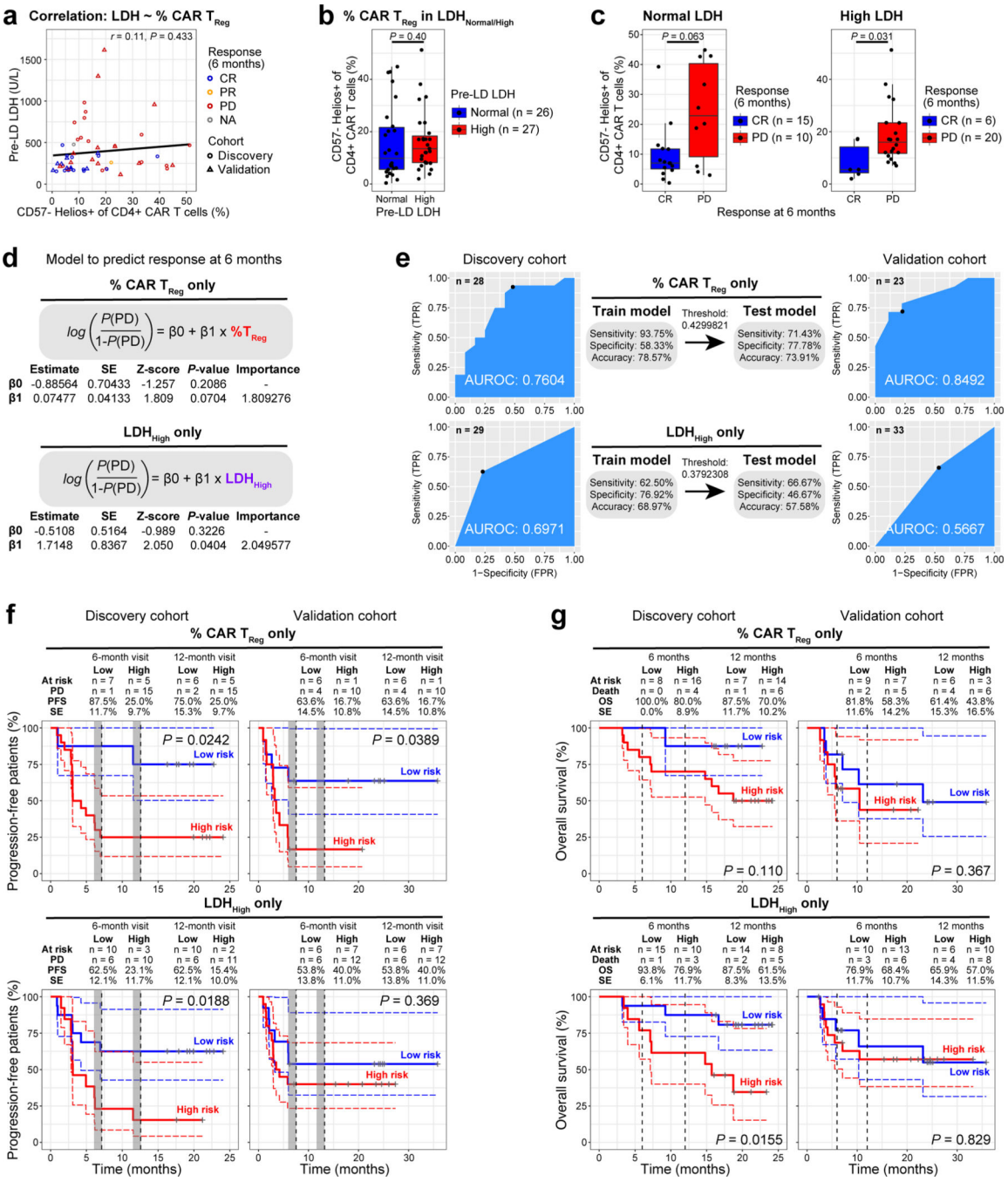

Extended Data Fig. 10. Risk of clinical progression based on either high LDH or CAR T_{Reg} fraction alone.

a, Pearson correlation between pre-LD LDH levels and percentage of $CD57^{-}$ $Helios^{+}$ (T_{Reg}-like) cells among $CD4^{+}$ CAR T cells in blood on day 7 post-infusion colored by response at 6 months (n = 53). *P*-value is from the correlation test. **b**, Percentage of CAR T_{Reg} cells separated by normal or high pre-LD LDH levels (n = 53). **c**, Percentage of CAR T_{Reg} cells in patients with CR or PD at 6 months with normal pre-LD LDH (*left*, n = 25) or high pre-LD LDH (*right*, n = 26). Boxplots in (b,c) show quartiles with a band at

median, whiskers indicating 1.5 IQR, and all observations overlaid as dots. *P*-values are from two-sided Mann-Whitney *U* test. **d**, Logistic regression models for predicting response at 6 months based on either percent of CAR T_{Reg} cells (*top*, n = 28), or whether pre-LD LDH levels were above normal (*bottom*, n = 29). Models were fit using all available data from the discovery cohort, with parameters shown below the formula. **e**, Performance of each model from (d) on discovery (*top*, n = 28; *bottom*, n = 29) and validation (*top*, n = 23; *bottom*, n = 33) cohorts. All available data not in the discovery cohort were used to test each model (Supplementary Table S5). AUROC, area under the receiver operating characteristic. **f-g**, Kaplan-Meier analysis of TTP (f) and OS (g) stratified by high *vs.* low risk using the models from (d) on cohorts from (e).

Supplementary Material

Refer to Web version on PubMed Central for supplementary material.

Acknowledgments

We thank Tara Murty and Cecilia Ramello for critical review of the manuscript. Robbie Majzner, Aidan M. Tousley, and Sabine Heitzeneder provided healthy T cells expressing the CD19-CD28ζ CAR construct. Monoclonal anti-FMC63 idiotype antibody was kindly provided by Bipulendu Jena and Laurence J. N. Cooper. This work was supported by the California Institute for Regenerative Medicine (Award: CLIN2–10846, PI: C.L.M.), the National Cancer Institute (5P30CA124435, C.L.M.; 2P01CA049605-29A1, C.L.M. and D.B.M.; U54-CA209971, S.K.P.), a sponsored research agreement with Kite Pharma, a subsidiary of Gilead Sciences (D.B.M.), and a St. Baldrick's/Stand Up 2 Cancer Pediatric Dream Team Translational Cancer Research Grant (C.L.M.). Stand Up 2 Cancer is a program of the Entertainment Industry Foundation administered by the American Association for Cancer Research. This study was also supported by the Virginia and D.K. Ludwig Fund for Cancer Research (C.L.M.). Z.G. was supported by fellowships from the Parker Institute for Cancer Immunotherapy and the Stanford Cancer Institute, an NCI-designated Comprehensive Cancer Center. Z.G., S.C.B., and C.L.M. are members of the Parker Institute for Cancer Immunotherapy, which supports the Stanford University Cancer Immunotherapy Program. The Illumina HiSeq 4000 used here was purchased with the NIH funds (award S10OD018220).

Z.G. is an inventor on two patent applications, holds equity in Boom Capital Ventures, and a consultant for Mubadala Ventures, GLG, AlphaSights, and Atheneum Partners, all of which are related to the cancer immunotherapy space. S.A.F. holds patents in the field of cell and gene therapy and serves on the scientific advisory boards for Alaunos Therapeutics and FreshWind Biotechnologies. D.B.M. holds a patent with Pharmacyclics supporting ibrutinib for chronic graft-versus-host disease, receives consulting or research fees or serves as an advisor for Pharmacyclics, Kite Pharma, Adaptive Biotechnologies, Novartis, Juno Therapeutics, Celgene, Janssen Pharmaceuticals, Roche, Genentech, Precision Bioscience, Allogene, and Miltenyi Biotec. C.L.M. is an inventor on numerous CAR T cell immunotherapy patent applications and received royalties for the CD22-CAR from the NIH following licensure to Opus Bio and Juno Therapeutics. C.L.M. is a cofounder of Lyell Immunopharma, Syncopation Life Sciences, and Link Cell Therapies, which are developing CAR-based therapies, and consults for Lyell, Syncopation, Link, Mammoth, Ensoma, NeoImmune Tech, Apricity, Nektar, Immatics, Glaxo Smith Kline, and Bristol Myers Squibb. None of the above interests were related to the research described in this manuscript.

Data availability

All data associated with this study can be accessed through the Stanford Digital Repository at https://purl.stanford.edu/qb215vz6111. Raw singe-cell sequencing data are available through the Gene Expression Omnibus (GEO accession number GSE168940) at: https://www.ncbi.nlm.nih.gov/geo/query/acc.cgi?acc=GSE168940.

References

1. Abramson JS, et al. Lisocabtagene maraleucel for patients with relapsed or refractory large B cell lymphomas (TRANSCEND NHL 001): a multicentre seamless design study. Lancet 396, 839–852 (2020). [PubMed: 32888407]
2. Schuster SJ, et al. Tisagenlecleucel in Adult Relapsed or Refractory Diffuse Large B cell Lymphoma. N Engl J Med 380, 45–56 (2019). [PubMed: 30501490]
3. Neelapu SS, et al. Axicabtagene Ciloleucel CAR T cell Therapy in Refractory Large B cell Lymphoma. N Engl J Med 377, 2531–2544 (2017). [PubMed: 29226797]
4. Maude SL, et al. Tisagenlecleucel in Children and Young Adults with B cell Lymphoblastic Leukemia. N Engl J Med 378, 439–448 (2018). [PubMed: 29385370]
5. Nastoupil LJ, et al. Standard-of-Care Axicabtagene Ciloleucel for Relapsed or Refractory Large B cell Lymphoma: Results From the US Lymphoma CAR T Consortium. J Clin Oncol 38, 3119–3128 (2020). [PubMed: 32401634]
6. Locke FL, et al. Long-term safety and activity of axicabtagene ciloleucel in refractory large B cell lymphoma (ZUMA-1): a single-arm, multicentre, phase 1–2 trial. Lancet Oncol 20, 31–42 (2019). [PubMed: 30518502]
7. Jacobson CA, et al. Axicabtagene Ciloleucel in the Non-Trial Setting: Outcomes and Correlates of Response, Resistance, and Toxicity. J Clin Oncol 38, 3095–3106 (2020). [PubMed: 32667831]
8. Locke FL, et al. Axicabtagene Ciloleucel as Second-Line Therapy for Large B cell Lymphoma. N Engl J Med 386, 640–654 (2022). [PubMed: 34891224]
9. Lee DW, et al. ASTCT Consensus Grading for Cytokine Release Syndrome and Neurologic Toxicity Associated with Immune Effector Cells. Biol Blood Marrow Transplant 25, 625–638 (2019). [PubMed: 30592986]
10. Neelapu SS, et al. Chimeric antigen receptor T cell therapy - assessment and management of toxicities. Nat Rev Clin Oncol 15, 47–62 (2018). [PubMed: 28925994]
11. Brown CE & Mackall CL. CAR T cell therapy: inroads to response and resistance. Nat Rev Immunol 19, 73–74 (2019). [PubMed: 30631206]
12. Deng Q, et al. Characteristics of anti-CD19 CAR T cell infusion products associated with efficacy and toxicity in patients with large B cell lymphomas. Nat Med (2020).
13. Rossi J, et al. Preinfusion polyfunctional anti-CD19 chimeric antigen receptor T cells are associated with clinical outcomes in NHL. Blood 132, 804–814 (2018). [PubMed: 29895668]
14. Fraietta JA, et al. Determinants of response and resistance to CD19 chimeric antigen receptor (CAR) T cell therapy of chronic lymphocytic leukemia. Nat Med 24, 563–571 (2018). [PubMed: 29713085]
15. Locke FL, et al. Tumor burden, inflammation, and product attributes determine outcomes of axicabtagene ciloleucel in large B cell lymphoma. Blood Adv 4, 4898–4911 (2020). [PubMed: 33035333]
16. Frank MJ, et al. Monitoring of Circulating Tumor DNA Improves Early Relapse Detection After Axicabtagene Ciloleucel Infusion in Large B cell Lymphoma: Results of a Prospective Multi-Institutional Trial. J Clin Oncol 39, 3034–3043 (2021). [PubMed: 34133196]
17. Majzner RG & Mackall CL. Tumor Antigen Escape from CAR T cell Therapy. Cancer Discov 8, 1219–1226 (2018). [PubMed: 30135176]
18. Zhang Z, et al. Point mutation in CD19 facilitates immune escape of B cell lymphoma from CAR-T cell therapy. J Immunother Cancer 8(2020).
19. Majzner RG, et al. Tuning the Antigen Density Requirement for CAR T cell Activity. Cancer Discov 10, 702–723 (2020). [PubMed: 32193224]
20. Lynn RC, et al. c-Jun overexpression in CAR T cells induces exhaustion resistance. Nature 576, 293–300 (2019). [PubMed: 31802004]
21. Norelli M, et al. Monocyte-derived IL-1 and IL-6 are differentially required for cytokine-release syndrome and neurotoxicity due to CAR T cells. Nat Med 24, 739–748 (2018). [PubMed: 29808007]

22. Gust J, et al. Endothelial Activation and Blood-Brain Barrier Disruption in Neurotoxicity after Adoptive Immunotherapy with CD19 CAR-T Cells. Cancer Discov 7, 1404–1419 (2017). [PubMed: 29025771]
23. Parker KR, et al. Single-Cell Analyses Identify Brain Mural Cells Expressing CD19 as Potential Off-Tumor Targets for CAR-T Immunotherapies. Cell 183, 126–142 e117 (2020). [PubMed: 32961131]
24. Taraseviciute A, et al. Chimeric Antigen Receptor T Cell-Mediated Neurotoxicity in Nonhuman Primates. Cancer Discov 8, 750–763 (2018). [PubMed: 29563103]
25. Chou CK & Turtle CJ. Insight into mechanisms associated with cytokine release syndrome and neurotoxicity after CD19 CAR-T cell immunotherapy. Bone Marrow Transplant 54, 780–784 (2019). [PubMed: 31431714]
26. Santomasso BD, et al. Clinical and Biological Correlates of Neurotoxicity Associated with CAR T cell Therapy in Patients with B cell Acute Lymphoblastic Leukemia. Cancer Discov 8, 958–971 (2018). [PubMed: 29880584]
27. Jena B, et al. Chimeric antigen receptor (CAR)-specific monoclonal antibody to detect CD19-specific T cells in clinical trials. PLoS One 8, e57838 (2013). [PubMed: 23469246]
28. Wei J, et al. The model of cytokine release syndrome in CAR T cell treatment for B cell non-Hodgkin lymphoma. Signal Transduct Target Ther 5, 134 (2020). [PubMed: 32728035]
29. Bendall SC, et al. Single-cell mass cytometry of differential immune and drug responses across a human hematopoietic continuum. Science 332, 687–696 (2011). [PubMed: 21551058]
30. Tibshirani R. Regression shrinkage and selection via the lasso. Journal of the Royal Statistical Society, Series B, 267–288 (1996).
31. Azuma M, Phillips JH & Lanier LL. CD28- T lymphocytes. Antigenic and functional properties. J Immunol 150, 1147–1159 (1993). [PubMed: 8381831]
32. Lun ATL, Richard AC & Marioni JC. Testing for differential abundance in mass cytometry data. Nat Methods 14, 707–709 (2017). [PubMed: 28504682]
33. Walker AJ, et al. Tumor Antigen and Receptor Densities Regulate Efficacy of a Chimeric Antigen Receptor Targeting Anaplastic Lymphoma Kinase. Mol Ther 25, 2189–2201 (2017). [PubMed: 28676342]
34. Kared H, Martelli S, Ng TP, Pender SL & Larbi A. CD57 in human natural killer cells and T-lymphocytes. Cancer Immunol Immunother 65, 441–452 (2016). [PubMed: 26850637]
35. Spiegel JY, et al. CAR T cells with dual targeting of CD19 and CD22 in adult patients with recurrent or refractory B cell malignancies: a phase 1 trial. Nat Med 27, 1419–1431 (2021). [PubMed: 34312556]
36. Stoeckius M, et al. Simultaneous epitope and transcriptome measurement in single cells. Nat Methods 14, 865–868 (2017). [PubMed: 28759029]
37. Hao Y, et al. Integrated analysis of multimodal single-cell data. Cell 184, 3573–3587 e3529 (2021). [PubMed: 34062119]
38. Kern F, et al. Distribution of human CMV-specific memory T cells among the CD8pos. subsets defined by CD57, CD27, and CD45 isoforms. Eur J Immunol 29, 2908–2915 (1999). [PubMed: 10508265]
39. Seo H, et al. TOX and TOX2 transcription factors cooperate with NR4A transcription factors to impose CD8(+) T cell exhaustion. Proc Natl Acad Sci U S A 116, 12410–12415 (2019). [PubMed: 31152140]
40. Scott AC, et al. TOX is a critical regulator of tumour-specific T cell differentiation. Nature 571, 270–274 (2019). [PubMed: 31207604]
41. Khan O, et al. TOX transcriptionally and epigenetically programs CD8(+) T cell exhaustion. Nature 571, 211–218 (2019). [PubMed: 31207603]
42. Alfei F, et al. TOX reinforces the phenotype and longevity of exhausted T cells in chronic viral infection. Nature 571, 265–269 (2019). [PubMed: 31207605]
43. Chen J, et al. NR4A transcription factors limit CAR T cell function in solid tumours. Nature 567, 530–534 (2019). [PubMed: 30814732]

44. Bengsch B, et al. Epigenomic-Guided Mass Cytometry Profiling Reveals Disease-Specific Features of Exhausted CD8 T Cells. Immunity 48, 1029–1045 e1025 (2018). [PubMed: 29768164]
45. Tirosh I, et al. Dissecting the multicellular ecosystem of metastatic melanoma by single-cell RNA-seq. Science 352, 189–196 (2016). [PubMed: 27124452]
46. Good CR, et al. An NK-like CAR T cell transition in CAR T cell dysfunction. Cell 184, 6081–6100 e6026 (2021). [PubMed: 34861191]
47. Lee DW, et al. T cells expressing CD19 chimeric antigen receptors for acute lymphoblastic leukaemia in children and young adults: a phase 1 dose-escalation trial. Lancet 385, 517–528 (2015). [PubMed: 25319501]
48. Sauter CS, et al. CD19 CAR T cells following autologous transplantation in poor-risk relapsed and refractory B cell non-Hodgkin lymphoma. Blood 134, 626–635 (2019). [PubMed: 31262783]
49. Shah NN, et al. Bispecific anti-CD20, anti-CD19 CAR T cells for relapsed B cell malignancies: a phase 1 dose escalation and expansion trial. Nat Med 26, 1569–1575 (2020). [PubMed: 33020647]
50. Wang X, et al. Phase 1 studies of central memory-derived CD19 CAR T cell therapy following autologous HSCT in patients with B cell NHL. Blood 127, 2980–2990 (2016). [PubMed: 27118452]
51. Kebriaei P, et al. Phase I trials using Sleeping Beauty to generate CD19-specific CAR T cells. J Clin Invest 126, 3363–3376 (2016). [PubMed: 27482888]
52. Lamure S, et al. Clinical and Product Features Associated with Outcome of DLBCL Patients to CD19-Targeted CAR T cell Therapy. Cancers (Basel) 13(2021).
53. Kim HJ, et al. Stable inhibitory activity of regulatory T cells requires the transcription factor Helios. Science 350, 334–339 (2015). [PubMed: 26472910]
54. Huehn J, Polansky JK & Hamann A. Epigenetic control of FOXP3 expression: the key to a stable regulatory T cell lineage? Nat Rev Immunol 9, 83–89 (2009). [PubMed: 19114986]
55. Lopez-Verges S, et al. CD57 defines a functionally distinct population of mature NK cells in the human CD56dimCD16+ NK-cell subset. Blood 116, 3865–3874 (2010). [PubMed: 20733159]
56. Abo T & Balch CM. A differentiation antigen of human NK and K cells identified by a monoclonal antibody (HNK-1). J Immunol 127, 1024–1029 (1981). [PubMed: 6790607]
57. Dolstra H, et al. Expansion of CD8+CD57+ T cells after allogeneic BMT is related with a low incidence of relapse and with cytomegalovirus infection. Br J Haematol 90, 300307 (1995).
58. Melenhorst JJ, et al. Decade-long leukaemia remissions with persistence of CD4(+) CAR T cells. Nature (2022).
59. Sheih A, et al. Clonal kinetics and single-cell transcriptional profiling of CAR-T cells in patients undergoing CD19 CAR-T immunotherapy. Nat Commun 11, 219 (2020). [PubMed: 31924795]

References (Methods only)

60. Cheson BD, et al. Recommendations for initial evaluation, staging, and response assessment of Hodgkin and non-Hodgkin lymphoma: the Lugano classification. J Clin Oncol 32, 3059–3068 (2014). [PubMed: 25113753]
61. Lee DW, et al. Current concepts in the diagnosis and management of cytokine release syndrome. Blood 124, 188–195 (2014). [PubMed: 24876563]
62. Long AH, et al. 4–1BB costimulation ameliorates T cell exhaustion induced by tonic signaling of chimeric antigen receptors. Nat Med 21, 581–590 (2015). [PubMed: 25939063]
63. Fienberg HG, Simonds EF, Fantl WJ, Nolan GP & Bodenmiller B. A platinum-based covalent viability reagent for single-cell mass cytometry. Cytometry. Part A : the journal of the International Society for Analytical Cytology 81, 467–475 (2012). [PubMed: 22577098]
64. Zunder ER, et al. Palladium-based mass tag cell barcoding with a doublet-filtering scheme and single-cell deconvolution algorithm. Nat Protoc 10, 316–333 (2015). [PubMed: 25612231]
65. Finck R, et al. Normalization of mass cytometry data with bead standards. Cytometry A 83, 483–494 (2013). [PubMed: 23512433]
66. Hahne F, et al. flowCore: a Bioconductor package for high throughput flow cytometry. BMC Bioinformatics 10, 106 (2009). [PubMed: 19358741]

67. Van Gassen S, et al. FlowSOM: Using self-organizing maps for visualization and interpretation of cytometry data. Cytometry A 87, 636–645 (2015). [PubMed: 25573116]

68. Stuart T, et al. Comprehensive Integration of Single-Cell Data. Cell 177, 1888–1902 e1821 (2019). [PubMed: 31178118]

69. Hafemeister C & Satija R. Normalization and variance stabilization of single-cell RNA-seq data using regularized negative binomial regression. Genome Biol 20, 296 (2019). [PubMed: 31870423]

70. Gillespie M, et al. The reactome pathway knowledgebase 2022. Nucleic Acids Res 50, D687–D692 (2022). [PubMed: 34788843]

71. Gu Z, Eils R & Schlesner M. Complex heatmaps reveal patterns and correlations in multidimensional genomic data. Bioinformatics 32, 2847–2849 (2016). [PubMed: 27207943]

72. Rowland M & Tozer TN Clinical Pharmacokinetics and Pharmacodynamics - Concepts and Applications, (Wolters Kluwer Health/Lippincott William & Wilkins, 2011).

73. Friedman J, Hastie T & Tibshirani R. Regularization Paths for Generalized Linear Models via Coordinate Descent. J Stat Softw 33, 1–22 (2010). [PubMed: 20808728]

74. Kuhn M. Building Predictive Models in R Using the caret Package. J Stat Softw 28, 1–26 (2008). [PubMed: 27774042]

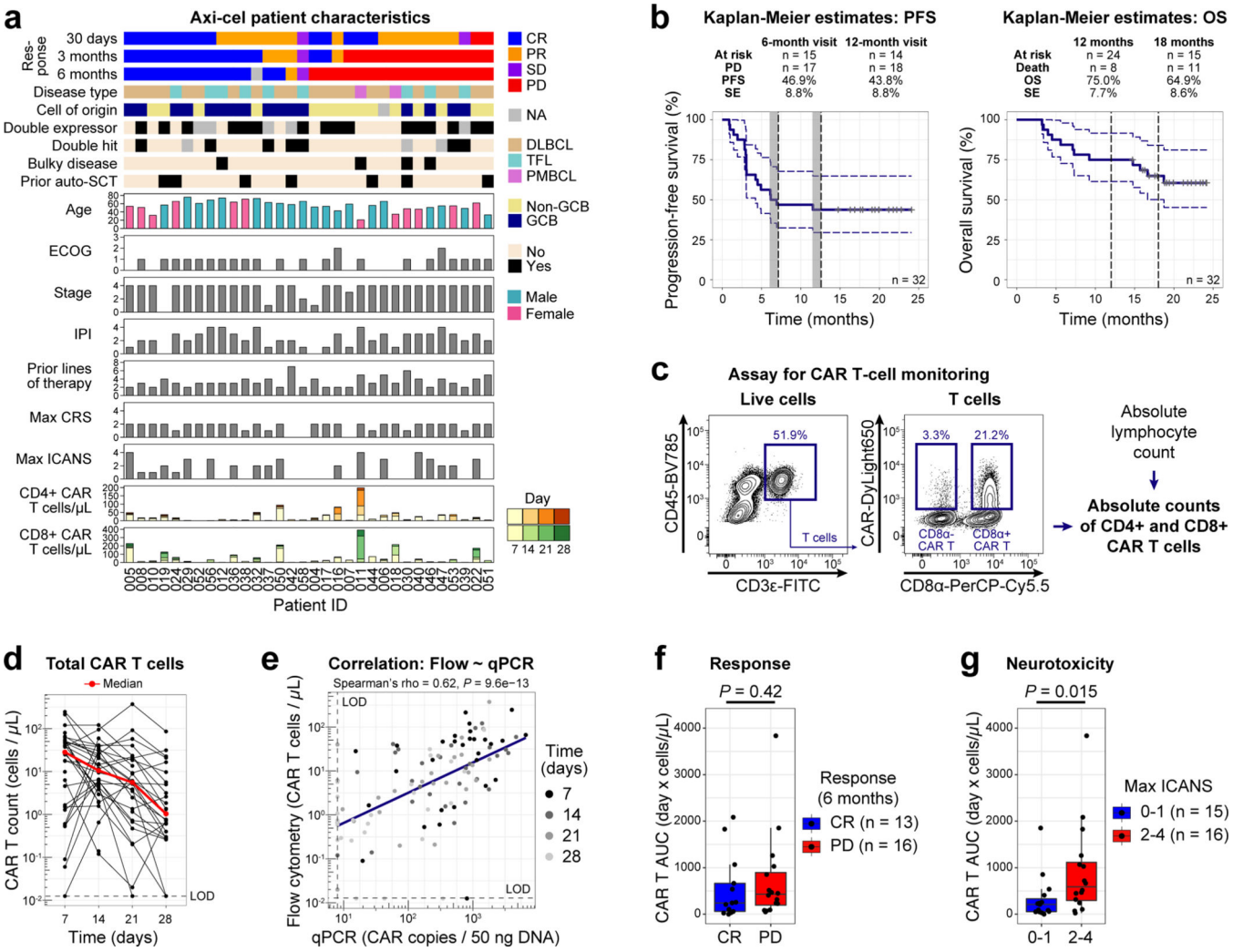

Fig. 1. Clinical response in LBCL patients treated with axi-cel is not associated with peripheral CAR T cell expansion.

a, Summary of clinical parameters for the study cohort of LBCL patients treated with axi-cel (n = 32). **b**, PFS (*left*) and OS (*right*) for the patient cohort following axi-cel infusion (n = 32). Patient 032 died in remission at 4.5 months post-infusion. Grey boxes show 6 and 12-month follow-up visit windows. Dashed lines indicate the end of each visit period, where survival estimates were calculated. SE, standard error. **c**, Flow cytometry assay for monitoring absolute counts of circulating $CD4^+$ and $CD8^+$ CAR T cells in axi-cel patients, gated as $CD3\varepsilon^+$ $CD4^+$ $CD8\alpha^-$ CAR^+ or $CD3\varepsilon^+$ $CD4^-$ $CD8\alpha^+$ CAR^+ events among single viable $CD45^+$ lymphocytes. An example partial gating scheme for patient 040 is shown. **d**, CAR T cell absolute blood counts on days 7, 14, 21, and 28 following axi-cel infusion (n = 32 patients, 128 observations). LOD, limit of detection. **e**, Spearman correlation in peripheral CAR T cell expansion between flow cytometry and qPCR assays (n = 31 patients, 109 observations). **f**, CAR T cell $AUC_{0–28}$ for patients in CR or PD at 6 months (n = 29; patients 042 and 058 had PR and SD at 6 months, patient 032 died from a non-progression related cause prior to 6 months). **g**, CAR T $AUC_{0–28}$ stratified by the maximum ICANS grade: 0–1 *vs.* 2–4 (n = 31; no $AUC_{0–28}$ data collected for patient 058). Boxplots in (f,g)

show quartiles with a band at median, whiskers indicating 1.5 interquartile range (IQR), and all observations overlaid as dots. *P*-values are from two-sided Mann-Whitney *U* test.

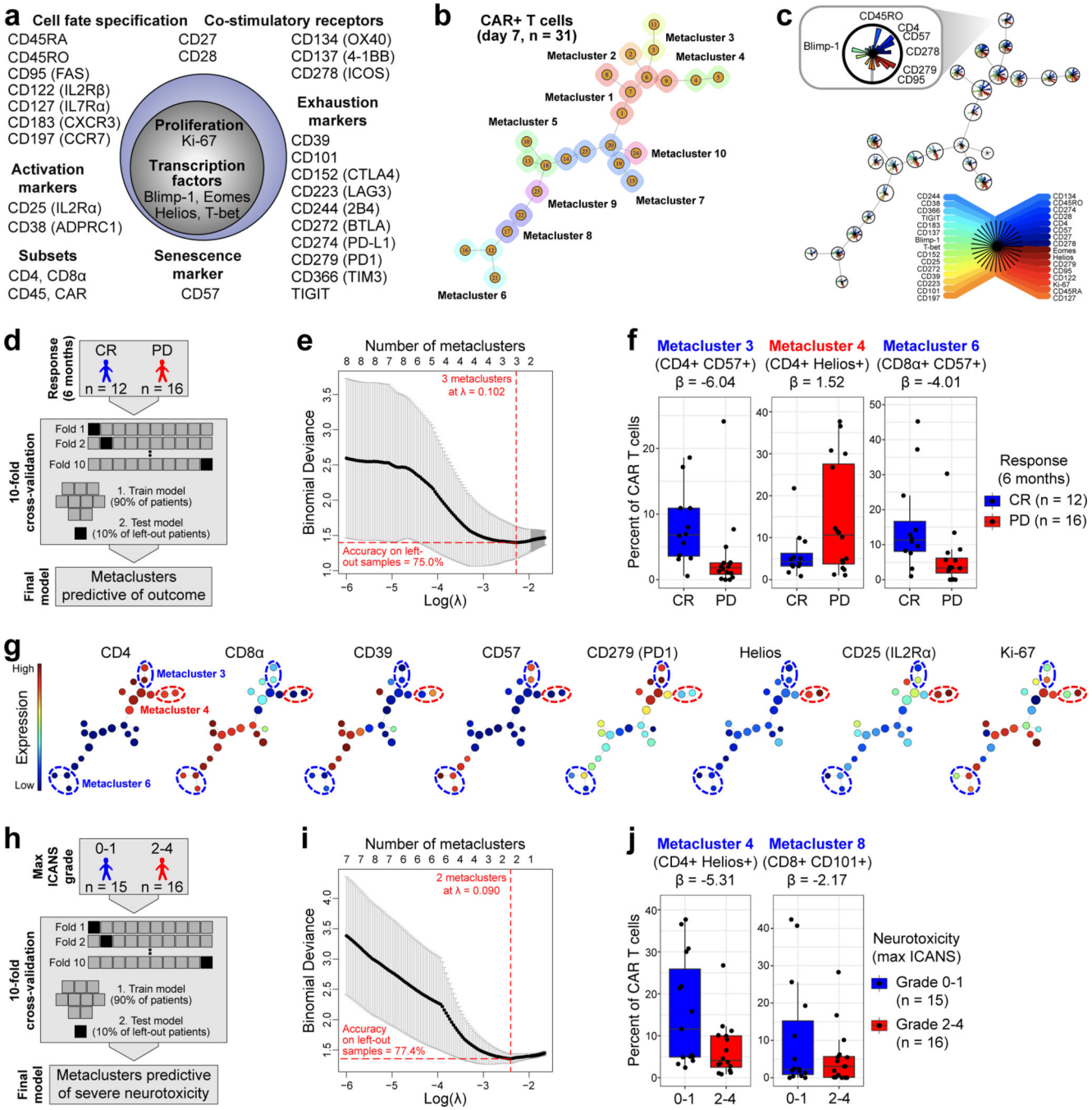

Fig. 2. CyTOF identifies metaclusters of circulating CAR T cells associated with long-term clinical response or neurotoxicity.

a, CyTOF panel covering 34 proteins. Quality control channels are not shown. **b**, Minimum spanning tree (MST) showing hierarchical consensus clustering of circulating CAR^+ T cells on day 7 following axi-cel infusion (n = 31 patients), with 25 clusters grouped automatically into 10 metaclusters. No CyTOF data were obtained for patient 038. **c**, Star plot showing MST from (b), with each cluster size scaled to represent its average abundance and colors indicating expression of each marker used for clustering. **d**, Schematic for building a lasso

model to predict clinical response as CR or PD at 6 months based on metacluster abundance from (c). **e**, Cross-validation results for model from (d), with red lines showing optimal model parameters. **f**, Relative abundance and b coefficients of 3 metaclusters selected by the lasso model for patients in CR or PD at 6 months (n = 28). **g**, Expression of 8 proteins overlaid onto MST from (c). **h**, Schematic for building a lasso model to predict maximum ICANS grade as 0–1 *vs.* 2–4 based on metaclusters from (c). **i**, Lasso cross-validation results for the model in (h), with red lines showing optimal model parameters. **j**, Relative abundance and β coefficients of 2 metaclusters selected by the lasso model in (h) (n = 31 patients). Boxplots in (f,j) show quartiles with a band at median, whiskers indicating 1.5 IQR, and all observations overlaid as dots.

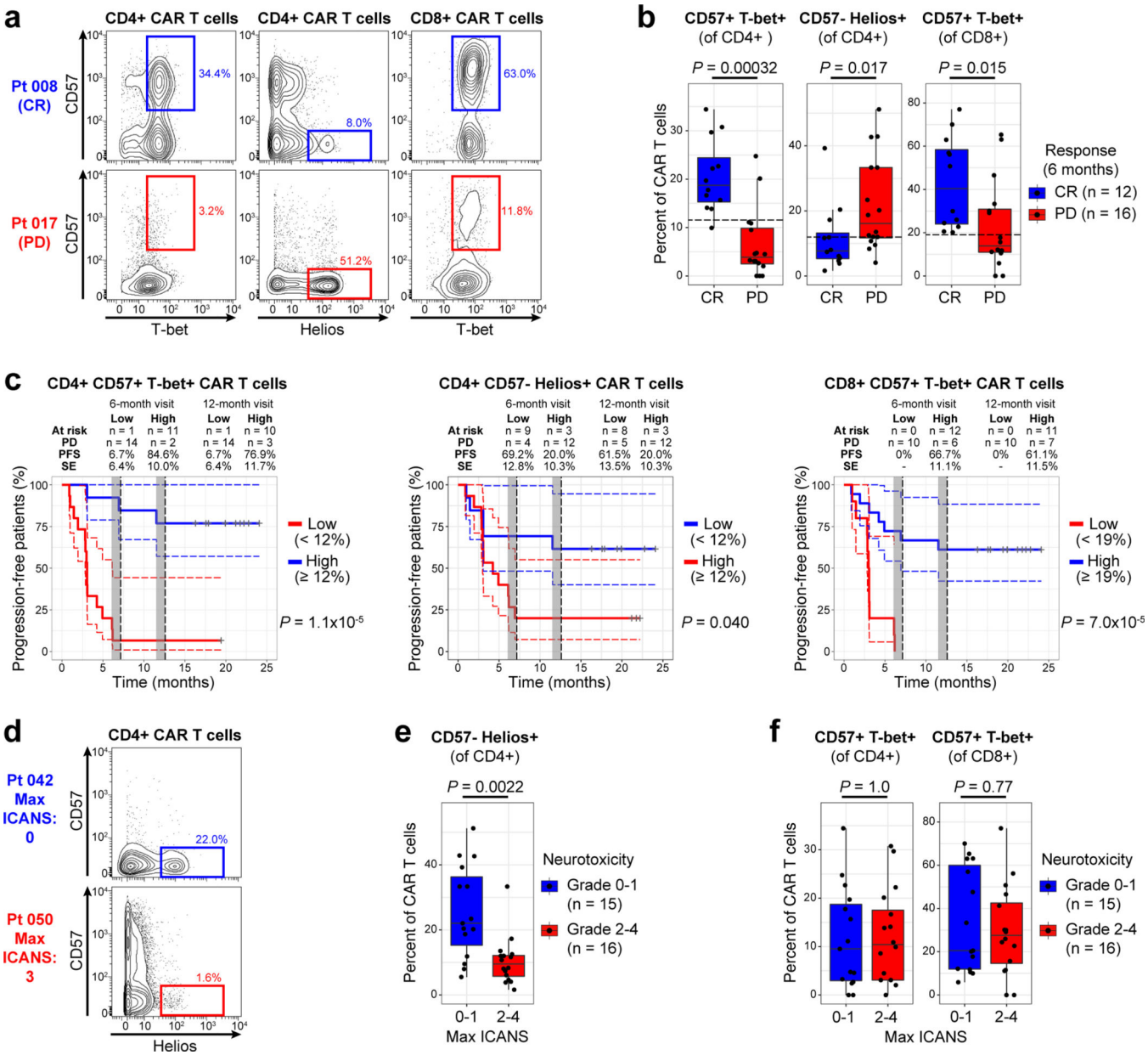

Fig. 3. Helios-expressing population of circulating CD4$^+$ CAR T cells on day 7 is associated with clinical progression and reduced neurotoxicity.

a, Gates defined based on 3 metaclusters identified by the lasso model for predicting clinical response (Fig. 2f). Contour plots show CyTOF data for CAR$^+$ T cells on day 7 from patients 008 (CR at 6 months) and 017 (PD at 6 months). **b**, Summary statistics for 3 populations as defined in (a) for patients in CR or PD at 6 months (n = 28). Dotted lines indicate separation between high and low percentages of CAR T cells in each population, with the thresholds selected based on the optimal response separation between the groups. **c**, Kaplan-Meier analysis of time to progression (TTP) stratified by high *vs.* low percentage of CAR T cells in each population, as shown in (b) (n = 28). Since clinical outcome was known during patient stratification, *P*-values need to be interpreted with caution. **d**, Gate from (a) defined

based on metacluster 4 identified by the lasso model for predicting severe neurotoxicity (Fig. 2j). Contour plots show CyTOF data for CAR^+ T cells on day 7 from patients 042 (max ICANS grade 0) and 050 (max ICANS grade 3). **e**, Percentage of circulating $CD57^-$ $Helios^+$ cells among $CD4^+$ CAR T cells on day 7 stratified by maximum ICANS grade (n = 31). **f**, Percentage of $CD57^+$ $T\text{-}bet^+$ cells among $CD4^+$ (*left*) and $CD8^+$ (*right*) CAR T cells on day 7 for patients with maximum ICANS grade 0–1 or 2–4 (n = 31). Boxplots in (b,e,f) show quartiles with a band at median, whiskers indicating 1.5 IQR, and all observations overlaid as dots. *P*-values are from two-sided Mann-Whitney *U* test.

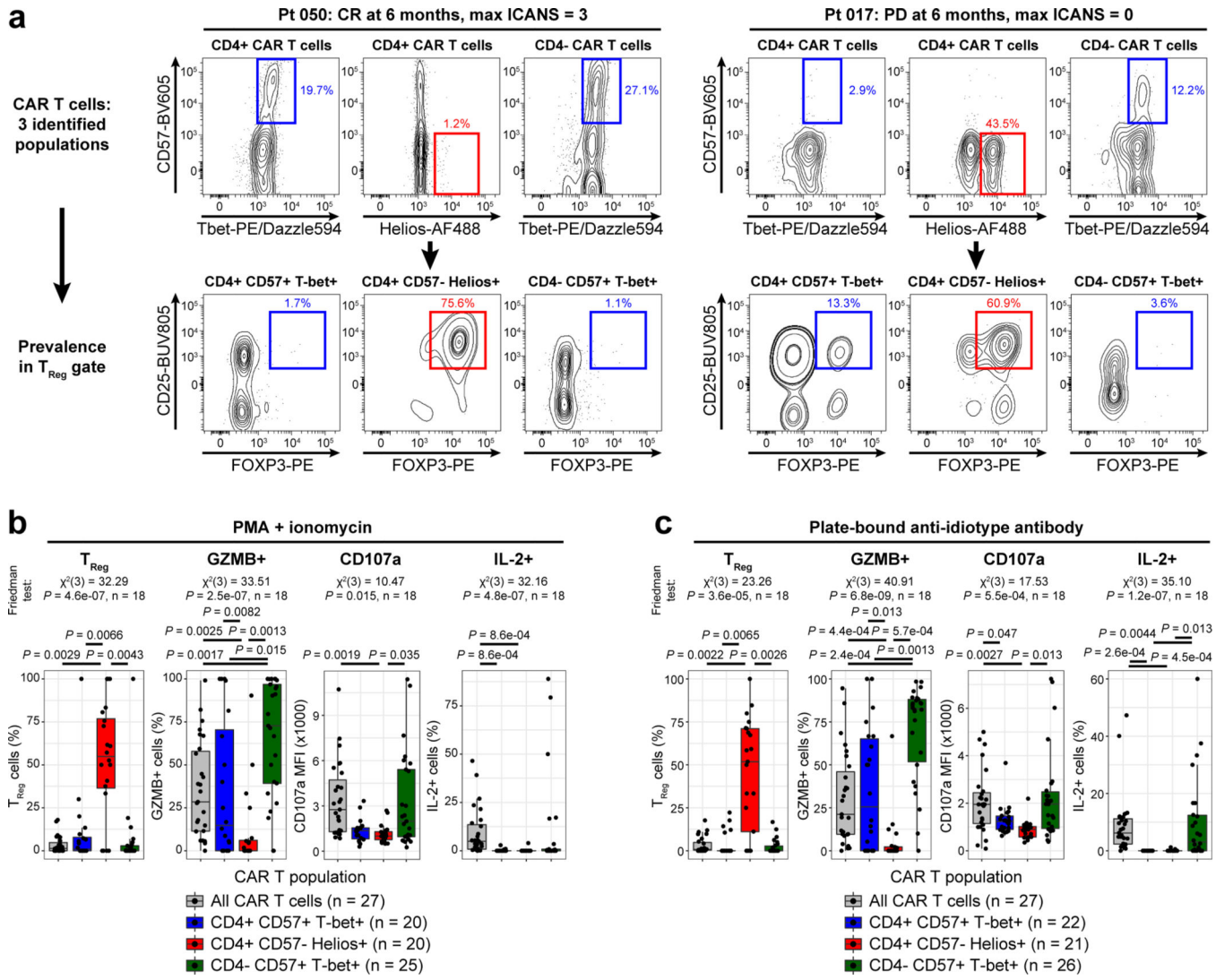

Fig. 4. CD4$^+$ CD57$^-$ Helios$^+$ CAR T cells express FOXP3 and are not cytotoxic.

Cryopreserved PMBCs from the patient cohort (day 7 after axi-cel infusion; n = 27) were incubated with either PMA and ionomycin, or plate-bound anti-idiotype antibody for 6 hours and analyzed by flow cytometry. **a**, *Top:* Contour plots show three identified populations among CAR$^+$ T cells from patients 017 and 050. *Bottom:* Percent of cells from each population falling into the FOXP3$^+$ CD25^{High} T_{Reg} gate. **b-c**, Summary statistics for CAR$^+$ T cells falling into T_{Reg}, GZMB$^+$, or IL-2$^+$ gates and surface CD107a MFI following stimulation with PMA and ionomycin (b) or plate-bound anti-idiotype antibody (c). Boxplots show quartiles with a band at median, whiskers indicating 1.5 IQR, and all observations overlaid as dots. *P*-values are from the Friedman test, followed by pairwise two-sided Wilcoxon signed-rank tests with Bonferroni correction to adjust for multiple hypothesis testing.

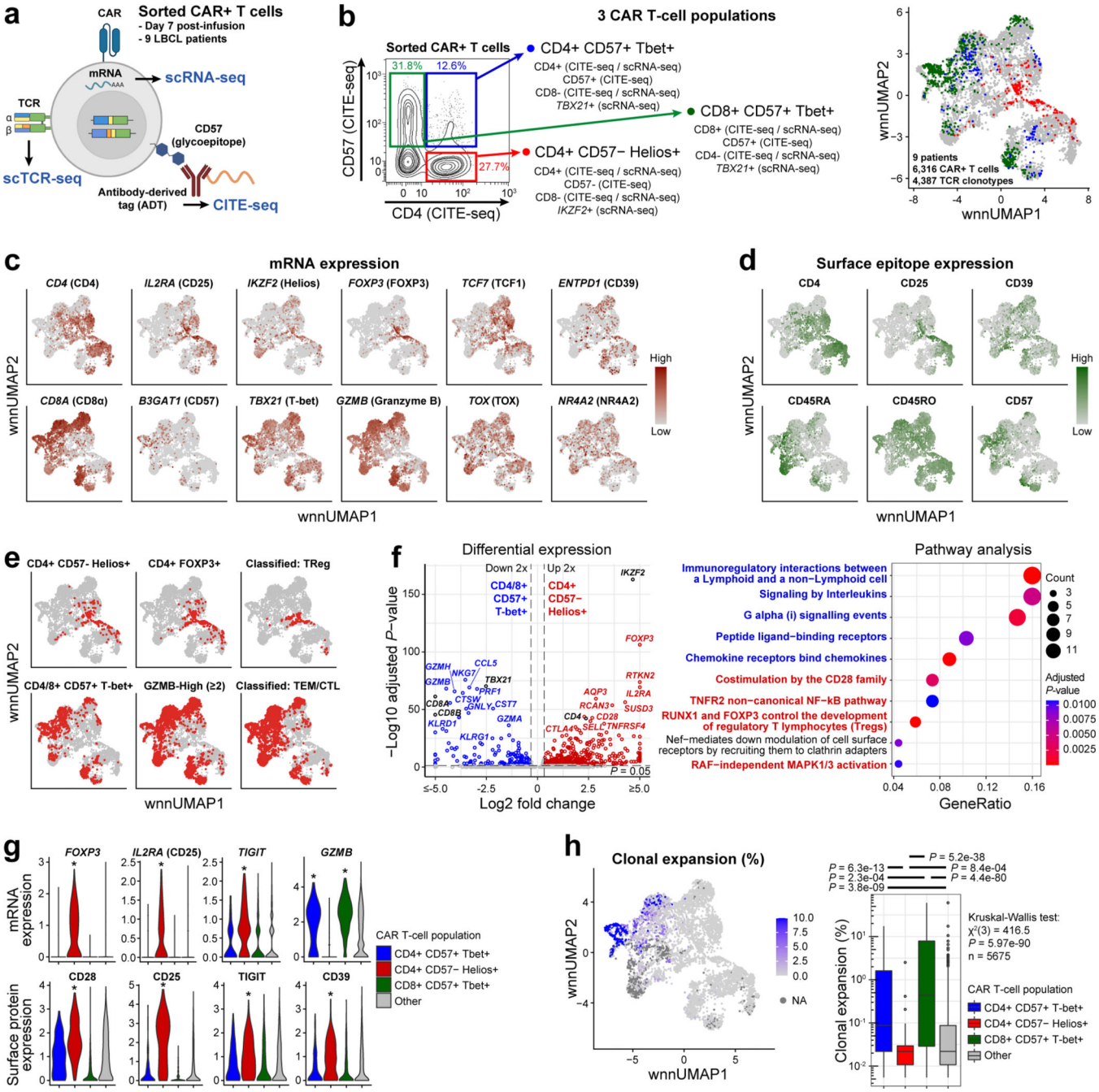

Fig. 5. Deep phenotyping with single-cell sequencing upholds T_{Reg} identity of CD4$^+$ CD57$^-$ Helios$^+$ CAR T cells.

a, CAR$^+$ T cells were sorted from 9 LBCL patients on day 7 following axi-cel infusion and analyzed by scRNA-seq, scTCR-seq, and CITE-seq. **b** *Left:* Contour plot and schematic show definitions of the 3 identified CAR T cell populations. *Right:* Identities of CAR T cell populations projected onto the weighted nearest neighbor UMAP (wnnUMAP) coordinates based on scRNA-seq and CITE-seq data (n = 6,316 cells). **c**, Expression of selected genes overlaid onto the wnnUMAP coordinates from (b). Protein encoded by each gene is shown in parentheses. **d**, Surface expression of selected proteins and CD57

(carbohydrate epitope) overlaid onto the wnnUMAP coordinates from (b). **e**, Indicated CAR T cell subsets highlighted in red on the wnnUMAP coordinates from (b). **f**, Volcano plot showing differentially expressed genes (*left*) and dot plot showing the top 10 differentially regulated pathways (*right*) comparing $CD4^+$ $CD57^-$ $Helios^+$ to $CD4^+$ $CD57^+$ $T\text{-}bet^+$ and $CD8^+$ $CD57^+$ $T\text{-}bet^+$ CAR T cell populations (n = 952 cells). Differentially upregulated genes and pathways are in red; downregulated genes and pathways are in blue; genes used to define each population and pathways with genes both up and downregulated are in black. **g**, Violin plots showing selected gene and surface protein expression in populations defined in (b) (n = 6,316 cells). Stars denote significant ($P < 0.05$) upregulation in the indicated population relative to all populations without stars. Other significant relationships are not denoted. **h**, TCR clonal expansion overlaid onto the wnnUMAP coordinates from (b) (*left*) and shown as a boxplot for each CAR T cell population (*right*). *P*-values in (g,h) were calculated using Kruskal-Wallis *H* test, followed by unpaired two-sided Wilcoxon-Mann Whitney *U* test applied to each treatment pair, with Bonferroni correction for multiple hypothesis testing.

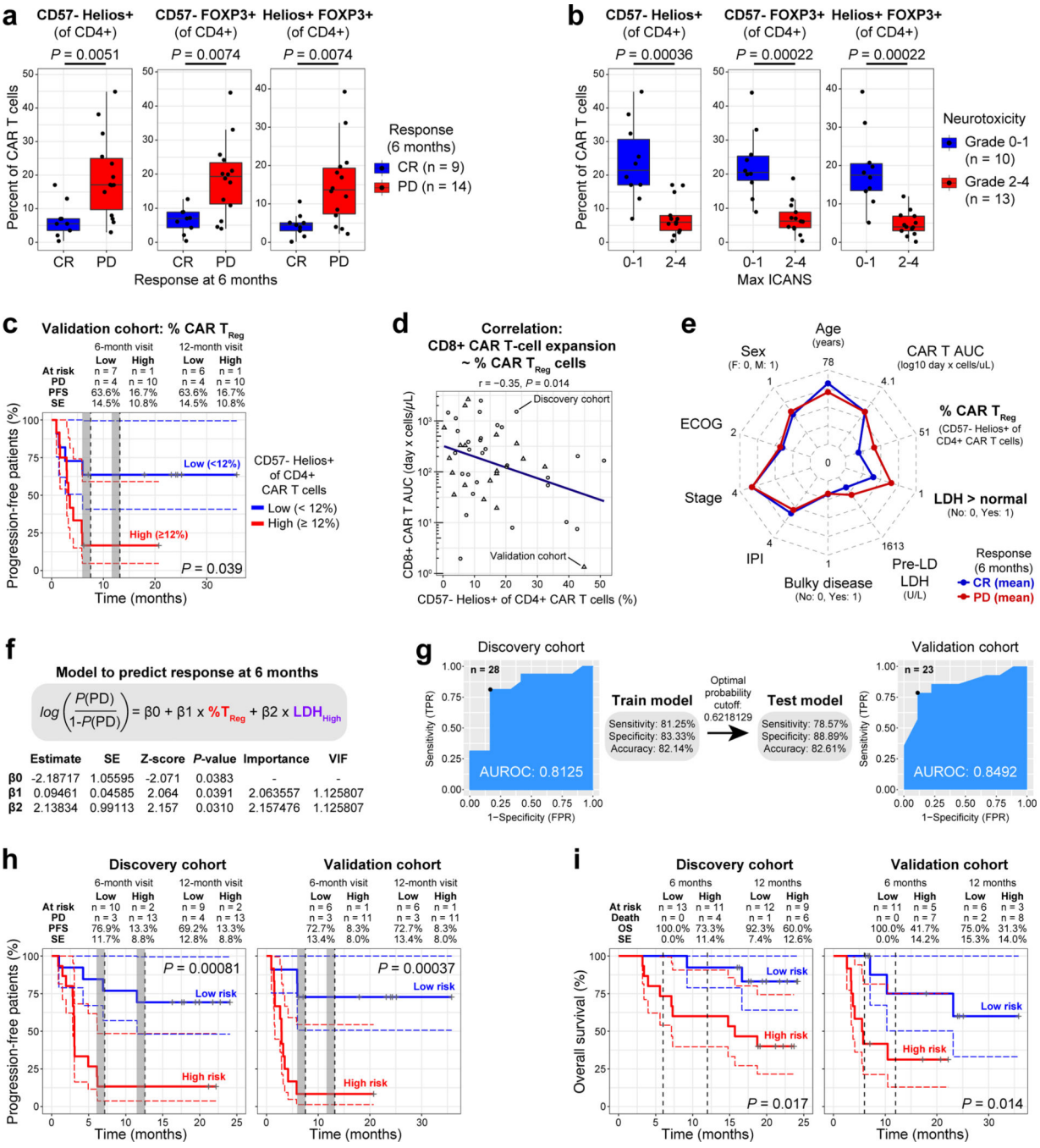

Fig. 6. CAR T_{Reg} cells and tumor burden surrogate identify patients with clinical progression.

a-b, Percentage of indicated populations among $CD4^+$ CAR T cells in blood on day 7 post-infusion in patients from the validation cohort (n = 23), separated by response at 6 month (a) or maximum ICANS grade (b). Boxplots show quartiles with a band at median, whiskers indicating 1.5 IQR, and all observations overlaid as dots. *P*-values are from two-sided Mann-Whitney *U* test. (**c**) Kaplan-Meier analysis of TTP stratified by high *vs.* low percentage of $CD57^-$ $Helios^+$ population among $CD4^+$ (T_{Reg}-like) CAR T cells using the threshold from the discovery cohort (Fig. 3c) (n = 23). **d**, Pearson correlation between

percentage of CAR T_{Reg} cells and log10 $AUC_{0–28}$ expansion of $CD8^+$ CAR T cells (n = 54). *P*-value is from the correlation test. **e**, Radar plot showing mean values for all patients in CR or PD at 6 months (n = 64). Each axis starts at 0 and ends at the maximum value observed. **f**, Logistic regression model for predicting response at 6 months based on two parameters: percent of CAR T_{Reg} cells and whether pre-LD LDH levels were above normal. Model was fit using the discovery cohort (n = 28), with parameters shown below the formula. Variance inflation factor (VIF) ≥5 indicates severe multicollinearity. **g**, Performance of the model from (f) on discovery (n = 28) and validation (n = 23) cohorts. AUROC, area under the receiver operating characteristic. **h-I**, Kaplan-Meier analysis of TTP (h) and OS (i) stratified by high *vs.* low risk using the model from (f) in cohorts from (g).